APPLICATION OF INSAR TO SALT MINE SUBSIDENCE

A Thesis
Presented to the Faculty of the Graduate School
of Cornell University
in Partial Fulfillment of the Requirements for the Degree of
Masters

by
Benjamin Rudolph Valentino
August 2016

ABSTRACT

We demonstrate the capability of Interferometric Synthetic Aperture Radar (InSAR) to characterize subsidence associated with salt mining in western New York State. We examine L-band Synthetic Aperture Radar (SAR) data from the Advanced Land Observing Satellite-1 (ALOS-1) for multiple overlapping satellite tracks spanning across the state. Significant subsidence is observed over the American Rock Salt Mine in Livingston County while no subsidence is observed at other locations of known salt mining.

We also document interferograms with significant signals associated with snow cover. Independent snow water equivalent models from the SNOw Data Assimilation System (SNODAS) by the NOAA National Weather Service's Hydrologic Remote Sensing Center (NOHRSC) allow us to confirm the association between observed phase changes and the presence of snow. For the purposes of measuring salt mine subsidence, images containing significant snow cover were not used in the time series analysis since effects from snow can bias results.

For the American Rock Salt Mine, we generated InSAR time series using a persistent scatterer approach for two independent overlapping tracks with data spanning the time period from 22 December, 2006 to 24 March, 2011. We compared out time series results to leveling data provided by the American Rock Salt Company. We observe maximum rates on order of ~8 cm/yr in the near-vertical satellite line-of-sight direction, with a sign consistent with subsidence. Additionally, we find that, despite the impact of dense vegetation and agriculture, the InSAR data quality is sufficient for resolving non-linear subsidence corresponding to the extension of the mining activity over time. The spatial pattern of InSAR-observed rates agree generally with the leveling data, except that rates determined by leveling are larger in areas of

maximum subsidence, with an average difference of ~1.5 cm/yr. We explore several potential explanations for this discrepancy, concluding that it may be an artifact of the different temporal sampling of each dataset.

BIOGRAPHICAL SKETCH

Benjamin Valentino is in his second year of study in the Department Earth and Atmospheric Sciences at Cornell University. In August, 2016 he will graduate with a MS degree in geophysics. He graduated from SUNY Oswego in 2014 with BS degrees in mathematics and geology.

ACKNOWLEDGMENTS

I thank the Earth Energy IGERT Program for funding me while at Cornell. I also thank the American Rock Salt Company for providing access to their leveling data assisting with my master's study. PALSAR data from the ALOS-1 satellite has been made available through agreements between the Japanese Space Agency (JAXA), NASA, and the Alaska Satellite Facility (ASF).

I thank my family for their support, my office mates for their company, Professor Keranen for her helpful contributions as one of my committee members, and my adviser for her thoughtful guidance and contributions.

TABLE OF CONTENTS

LIST OF FIGURES

LIST OF TABLES

LIST OF SYMBOLS

$\vec{B}$	Baseline vector
$B_{\perp}$	Perpendicular baseline
$\widehat{l_1}$	Satellite unit look vector
$\vec{D}$	Surface displacement vector
λ	Radar wavelength
ϕ	Interferometric phase
θ	Satellite look angle
ρ_i	Satellite range distance
d_i	SAR scenes
(d_i, d_j)	SAR date pair combinations
ϕ_d	Surface displacement contribution to interferometric phase
ϕ_t	Topographic contribution to interferometric phase
ϕ_o	Orbital error contribution to interferometric phase
ϕ_α	Radar path delay contribution to interferometric phase
ϕ_c	Thermal noise and co-registration error contribution to interferometric phase
ϕ_{tot}	Total interferometric phase
ϕ_{res}	Residual from difference of filtered and non-filtered interferometric phase
ϕ_f	Filtered interferometric phase
γ	Interferometric phase variance
ϕ_k	Down-looked interferometric phase
$w_{i,j,k}$	Reciprocal of interferometric phase variance
a_l	Number of down-looks in azimuth
r_l	Number of down-looks in range
x_l	Down-looked interferogram dimension in range
y_l	Down-looked interferogram dimension in azimuth
G	Design matrix for least squares inversion
U	Matrix of Eigen vectors from singular value decomposition
V	Matrix of vectors spanning model space for singular value decomposition
S	Matrix of singular values from singular value decomposition
p	Matrix rank
G^{-g}	Generalized least squares solution
V_p	Truncated matrix of vectors spanning model space for singular value decomposition
U_p	Truncated matrix of Eigen vectors from singular value decomposition
S_p	Truncated matrix of singular values from singular value decomposition
R_m	Model resolution matrix
σ_r	Standard deviation of residuals from cumulative deformation inversion
r	Residuals from cumulative deformation inversion
$\bar{r}$	Mean of residuals from cumulative deformation inversion
r_{los}	Line of sight average rates
t_i	Time of each SAR scenes
δ	Residual from least squares inversion for average rates
$\sigma_{r_{los}}$	Standard deviation of residual from least squares inversion for average rates

N	Number of data points in resampled average rate maps
N_{patch}	Number of fault patches used for least squares inversion
G_i	Green's matrices for least squares fault slip inversion for each rate map
C_{d_i}	Inverse Cholesky factorization of data variance matrix
d_i	Vectors of resampled average rates for each satellite track
m_{model}	Vector of model parameters for least squares inversion
κ	Smoothing matrix in least squares solution
η	Damping matrix in least squares solution
λ_s	Smoothing factor for least squares solution
β	Damping factor for least squares solution

CHAPTER 1

INTRODUCTION

Salt is an important global commodity, used for food preservation/flavoring, chemical manufacturing, agricultural treatment, and road ice maintenance. Due to its importance, much effort has gone into the extraction of salt from both the surface and subsurface. Modern salt production in the northeast United States involves subsurface mining, and, like all subsurface mining operations, has associated risks. The stability of mining operations is fundamental to the continued development of the salt industry; however, prediction of salt mine behavior in response to different mining practices is challenging. Monitoring mining conditions in real-time or near-real-time can be a key component of efforts aimed at ensuring the safety of the mine workers and operations.

Observations of surface subsidence can be used to assist in the monitoring of mine stability – decision-making at the mine can be guided by whether the observed subsidence is similar to that expected in response to mine activity or if it exceeds those expectations. Surface subsidence can also cause damage to infrastructure; hence, subsidence monitoring is also useful for assessing potential problems before they become too severe (i.e., requirements for road maintenance). Satellite based geophysical remote sensing methods (e.g., Interferometric Synthetic Aperture Radar, or InSAR) can provide spatially and (in the future) temporally dense measurements of ground displacements.

1.1 Thesis Organization

This thesis is organized as follows. Chapter 2 covers the regional geology of western New York and the subsurface salt resources of New York State. A discussion of subsurface salt mining techniques as well as the extent of salt mining is also covered in Chapter 2. Chapter 2 finishes with a brief discussion of the mechanical behavior of rock salt, subsidence induced from subsurface excavations, and lastly covers a few case studies of salt mine subsidence and collapse including the Retsof, Wieliczka, and Varangeville Salt Mines. Chapter 3 introduces the geophysical remote sensing technique used in this thesis (InSAR), explains how it is applied, and covers some of the governing principles of the technique. Chapter 4 discusses the methods used for data processing and time series generation. Chapter 5 covers the data used in this thesis, results from data processing, and analyses applied for studying salt mine subsidence including comparisons of InSAR data with external datasets for accuracy checks and modeling. Chapter 5 also documents the effects of snow in the data with comparisons to independent datasets, and motivates our need to use independent snow cover models to cull out SAR images that may otherwise bias our results.

CHAPTER 2

SALT AND SALT MINING IN NEW YORK

2.1 Salt mining in NY State

Salt has been important in New York over much of the state's history, with the earliest commercial production of salt from salt springs in the Syracuse area during the late 1700's (Sanford, 1996). Methods of salt production eventually moved underground, and the rock salt mining industry has had a significant presence in New York State since major subsurface salt resource discoveries in 1878 (Briggs, 1996). The first commercial scale subsurface extraction of salt first occurred in 1881 and involved solution mining (Briggs, 1996). Since then, development of solution wells and room and pillar mines (mining styles described below) has been widespread, contributing greatly to the national production of salt. In 2013, New York State ranked third in salt production in the United States, accounting for 17% of national salt production (Bolen, 2015). In 2004, the combined value of solution and room and pillar salt products was estimated to be about $301 million for a total 6.4 million tons of salt produced (NYSDEC, undated).

The largest use of rock salt in New York State is for ice control, followed by chemical manufacturing, and then table salt, food processing, and agriculture uses (Bolen, 2015). The quality and, therefore, the end use of salt depend greatly on the production technique (solution versus room and pillar) used for extraction. Brine from solution mines is generally more pure, and is either used directly for chemical manufacturing or is refined through evaporation plants for food products, table salt, and chemical and pharmaceutical manufacturing (Briggs, 1996;

Sanford, 1996). Salt acquired from room and pillar mining is generally less refined, and is used mostly for snow and ice control or chemical manufacturing (Briggs, 1996).

Like all subsurface mining activity, the subsurface production of rock salt, which has occurred globally over much of the history of human civilization (e.g., Baar, 1977), has a number of associated hazards. Hazards to human life are frequently encountered in room and pillar mining as heavy equipment is routinely used and ceiling collapses do occur. Mine collapses resulting in subsidence and/or flooding of the mining operations can also produce environmental damage in addition to the financial losses sustained by the mine and interruption of supply to users.

This chapter covers the regional geology and distribution of commercial scale salt resources in New York State. The different types of mining methods used for salt extraction, and the distribution of mines in New York State will be discussed in addition to brief sections on the mechanical behavior of rock salt and subsidence associated with subsurface mining. The last section of this chapter will cover important case studies of both salt mine subsidence and catastrophic collapses.

2.1.1 Regional geology and salt resources of NY

The regional geology of western-central NY consists of Paleozoic sedimentary strata contained within the northern Appalachian Basin. The strata thicken towards the south-central part of the state, with maximum thickness over 13,000 feet, and gradually thin towards the northern and eastern ends of the state. The extent of the sedimentary strata is limited to the north by the highlands region with a thin east-west band of Silurian formations outcropping along the boundary (*Figure 1*) (Lugart et al., 2006).

Major salt bearing rock units are contained in the Silurian Salina Group. The Salina Group underlies a large portion of the northern Appalachian and Michigan Basins extending across much of New York, Pennsylvania, West Virginia, Ohio, Michigan, and southern Ontario. The total extent of salt is estimated to cover approximately 100,000 square miles with an average thickness of 150 feet making the Salina salt one of the largest bodies of rock salt in the world (Pierce and Rich, 1962). The Salina Group reaches a maximum thickness of about 3000 feet in the Michigan Basin and at the New York – Pennsylvania State border in the Appalachian Basin. The Salina Group is comprised of shales, dolomite, limestone, salt, gypsum, and anhydrite with largely shales at the eastern and northern ends of the strata. Salt is found in multiple beds throughout the group, with maximum salt thickness located at the center of the Michigan Basin (Pierce and Rich, 1962).

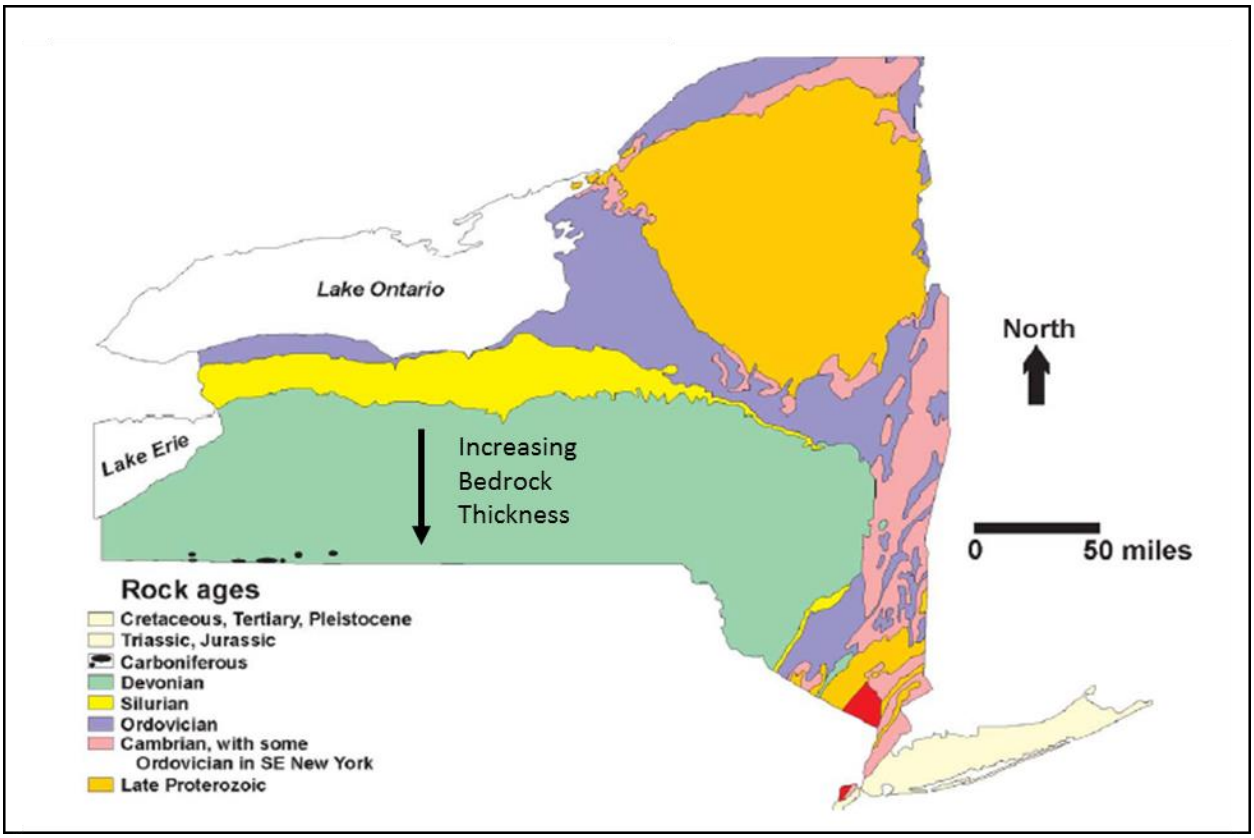

Figure 1: Generalized bedrock geology of New York State (From Lugart et al., 2006).

The Salina Group in New York State dips shallowly to the south and outcrops in a narrow band in the northern end of the western part of the state. The top of the Group is approximately 5000 feet deep at the NY-PA border, coincident with maximum aggregate salt thickness of about 800 feet (Pierce and Rich, 1962). Starting from the base of the group the Salina in NY is broken into five formations including the Pittsford Shale, the Vernon Shale, the Syracuse Salt, the Camillus Shale, and the Bertie Limestone (*Figure 2*). The Pittsford shale, not shown in the stratigraphic section in Figure 2, is only about 20 feet thick at maximum. Major salt layers in the region are located in the Syracuse and Vernon formations with most salt residing in the Syracuse formation. However, there are a number of salt layers within the Vernon Shale of significant thickness (*Figure 3*) which are currently being mined in western NY (Pierce and Rich, 1962; Yager et al., 2001).

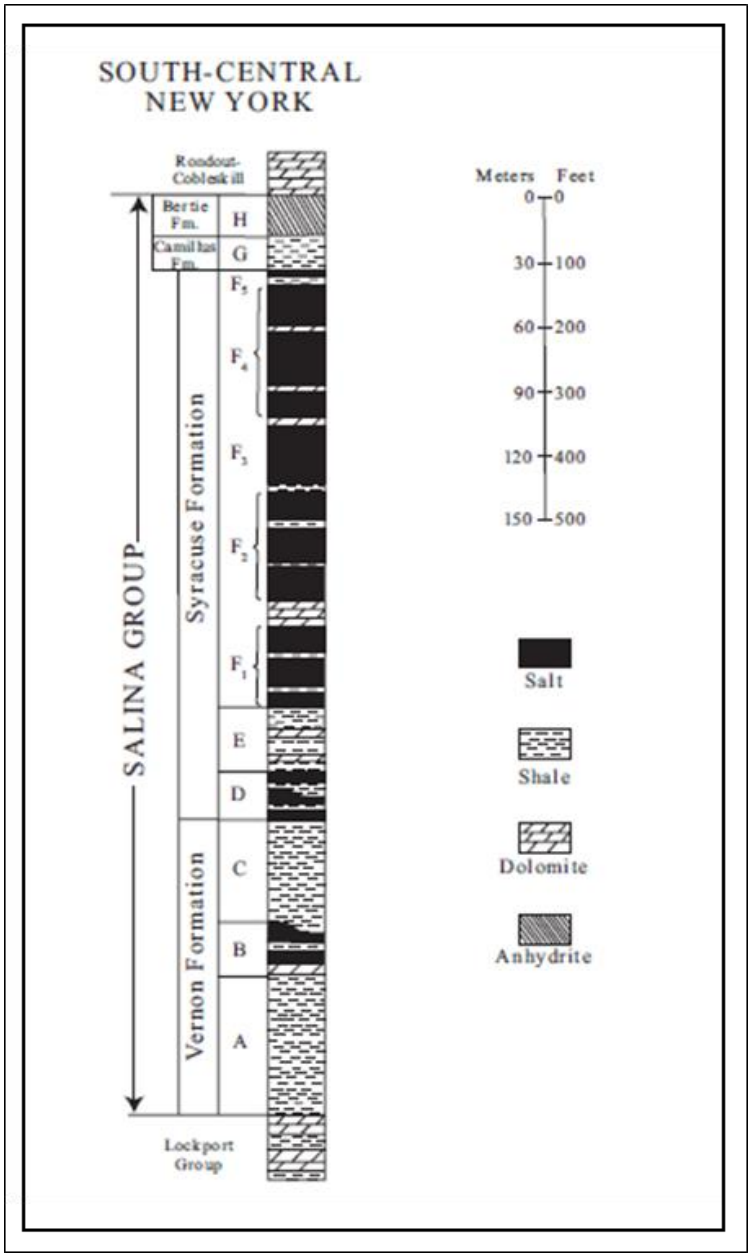

Figure 2: Generalized stratigraphic section of the Salina Group in South-Central New York (From Lugart et al., 2006).

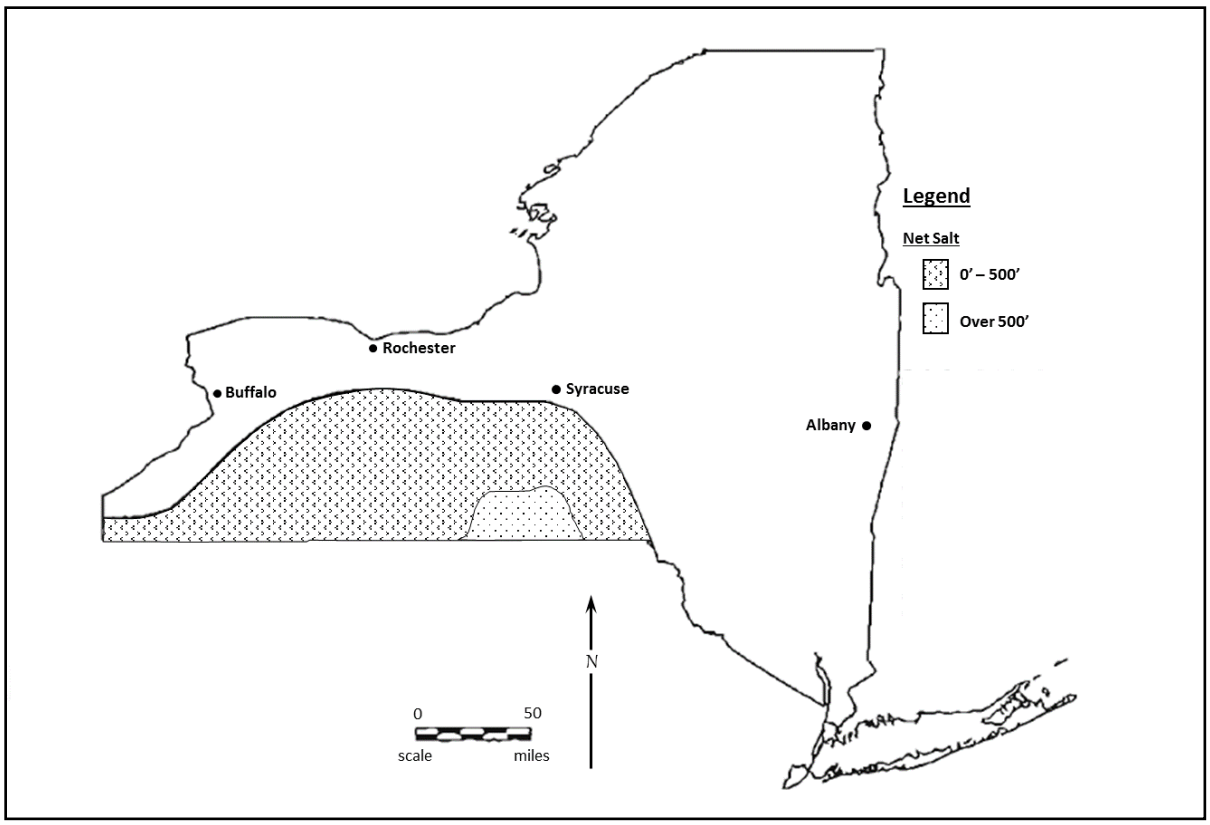

Figure 3: Distribution of salt deposits of commercial scale thickness in New York State (From Briggs, 1996).

2.1.2 Salt Mining Methods

The two primary methods of salt extraction include solution mining and room and pillar mining. For solution mining, water is injected into a salt layer through cased wells, and the resulting brine is pumped to the surface (Briggs, 1996; Sanford, 1996). Withdrawal of the brine can occur through the injection well (single well system) or through other wells connected via the solution cavity (multi-well system). Often solution mining fields start of as single well systems and transition to multi-well systems as the connectivity of the cavities increases (Briggs, 1996). A number of technologies commonly found in the oil industry are also applied to solution mines. Wells are cased to protect aquifers, hydrofracturing is employed to increase cavern connectivity, and horizontal drilling has been used in some solution fields (Sanford, 1996).

As cavities develop, water preferentially dissolves salt near the roof, increasing the area of unsupported ceiling. This increases the chance of collapse. Roof padding is a method employed to mitigate dissolution of the cavity roof and to better control the growth of the cavity. Air or oil is injected with fresh water which creates a barrier between the water and the roof (Sanford, 1996).

Room and pillar mining is a method developed for laterally extensive horizontally bedded units (Hamrin, 2001). Rooms (stopes) are excavated horizontally into the salt layer through mechanical or explosive means while leaving some of the unit intact (pillars) between adjacent stopes (Hamrin, 2001; Briggs, 1996). The spacing and size of the pillars are designed to optimize the quantities of salt extracted while providing sufficient support to the overlying strata (Hamrin, 2001). The ratio of the cross-sectional area of the mine rooms to the mine pillars is called the extraction ratio (Kratzsch, 1983). The extraction ratio is an important factor controlling the rate of convergence in the mine rooms, and often extraction ratios of about 40 – 50% are used (Kratzsch, 1983). Generally, some salt is left in place on the floor and ceiling of the mine rooms to mitigate contamination of the rock salt product with the over and underlying strata (Briggs, 1996).

A variant of the room and pillar method is the yield pillar method (e.g., Jeremic, 1994; Yavuz, 2001). Instead of requiring that each pillar support the entire load removed in the immediately adjacent rooms (tributary load model), this approach uses a combination of very strong (abutment) pillars with much smaller (yielding) pillars that will rapidly yield under the load of the overburden. This yielding results in a stress arch with a height that is dependent on the geometry of the pillars – the distance between the strong abutments must be small enough that the roof strata can support the overburden load above the arch. This reduces the load on the

yield pillars so that they only have to support the load of the material beneath the stress arch. The yield pillar technique, which was primarily developed in coal mine environments, is potentially capable of producing more stable mining environments provided that appropriate dimensions of the yield pillars are chosen (e.g., Yavuz, 2001).

2.1.3 Distribution of Salt Mining in NY

Salt mining occurs in a number of locations in the western part of New York State and includes both solution mining and conventional room and pillar mining methods. Solution mining is currently active at two and three locations in Schuyler and Wyoming Counties respectively (*Figure 4*) (NYSDEC). Three room and pillar mines are located throughout the state (*Figure 4*). Two are in Livingston County (Retsof and American Rock Salt Mines) and the third is located underneath Cayuga Lake in Tompkins County (Cayuga Mine). The American Rock Salt and Retsof mines are two of the largest salt mines in the country (Yager et al., 2001; Bolen, 2015), however, the Retsof Mine has been out of commission since 1995 due to catastrophic ceiling failure and extreme flooding (Nieto and Young, 1998). The active rock salt mines, American Rock Salt (targets of research presented here) and Cayuga mines, have a net production capacity of 6900 thousand short tons per year, and produce salt principally for road ice maintenance (Bolen, 2015).

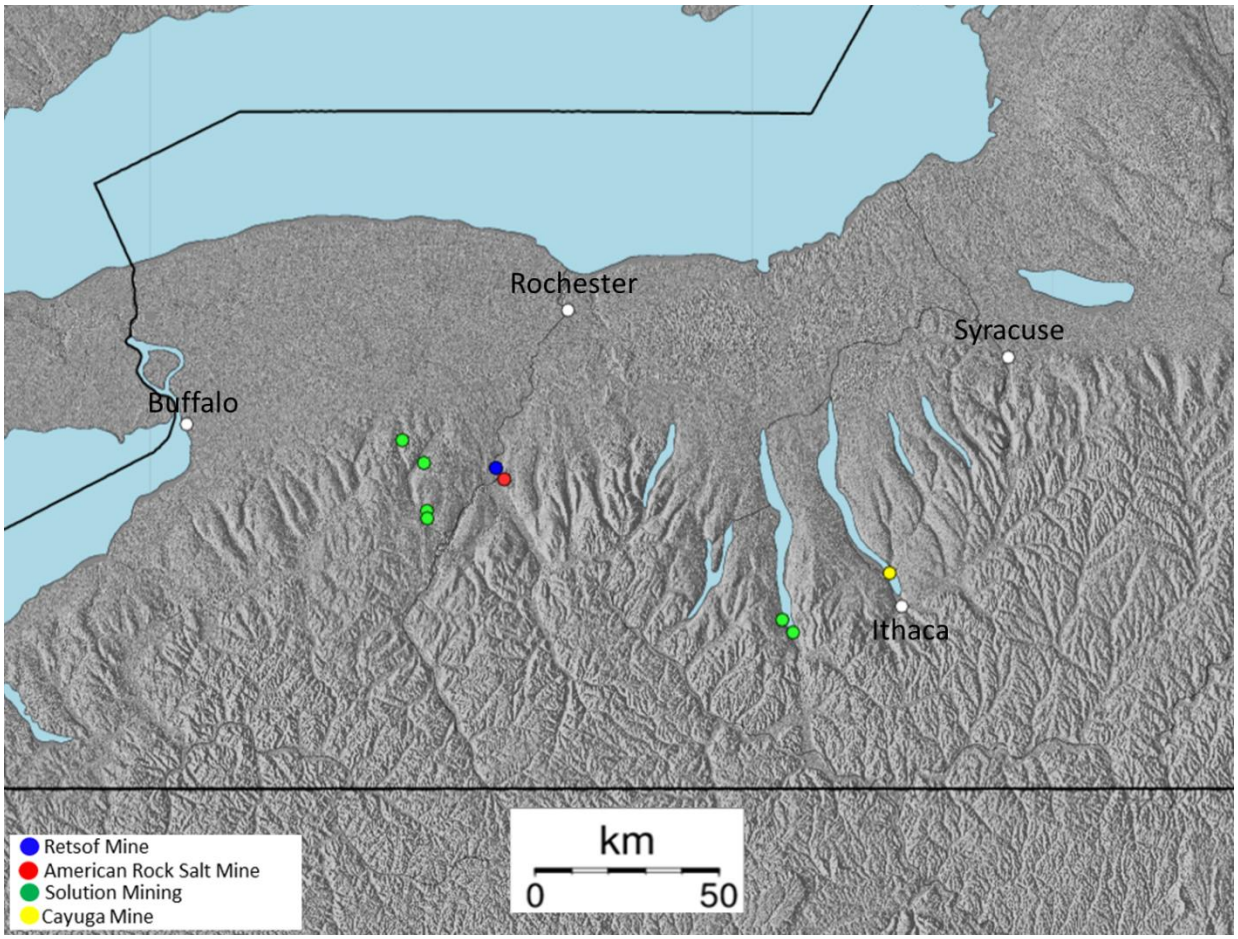

Figure 4: Regional map of western NY with shaded relief and locations of room and pillar salt mines indicated by colored dots.

2.2 Mechanical properties of rock salt

To characterize the stability of a mine and/or to understand observations of subsidence associated with a mine, it is important to begin with an understanding of the mechanical behavior of rock salt. The rock salt response to an applied load can be partitioned into four stages: immediate elastic response, primary creep, secondary creep, and (sometimes) tertiary creep (e.g., Swift and Reddish, 2005; Wittke, 2014). In the case of a mine, the applied load can be understood as the increase in load supported by the remaining pillars after the rooms have been excavated. There is an initial elastic response of the rock salt immediately following the application of the load (Swift and Reddish, 2005; Baar, 1977; Jaeger et al., 2007). The primary

creep stage is characterized by high but decreasing deformation rates due to strain hardening, which transitions to constant deformation rates in the secondary creep stage (steady state creep). Tertiary creep occurs when deformation rates increase, preceding failure or damage of the specimen (e.g., Swift and Reddish, 2005; Wittke, 2014; Baar, 1977; Jaeger et al., 2007). A typical laboratory-derived strain versus time curve for a material under a constant applied load is shown in Figure 5.

Rock salt undergoing steady state creep can proceed to tertiary creep and failure in cases where the applied load is greater than the uniaxial yield strength of the rock (Wittke, 2014). It has been found in many in situ observations that rock salt can remain in steady state creep seemingly for an indefinite period of time (Baar, 1977; Swift and Reddish, 2005), even in cases where extrapolation of laboratory results would have suggested the transition to tertiary creep.

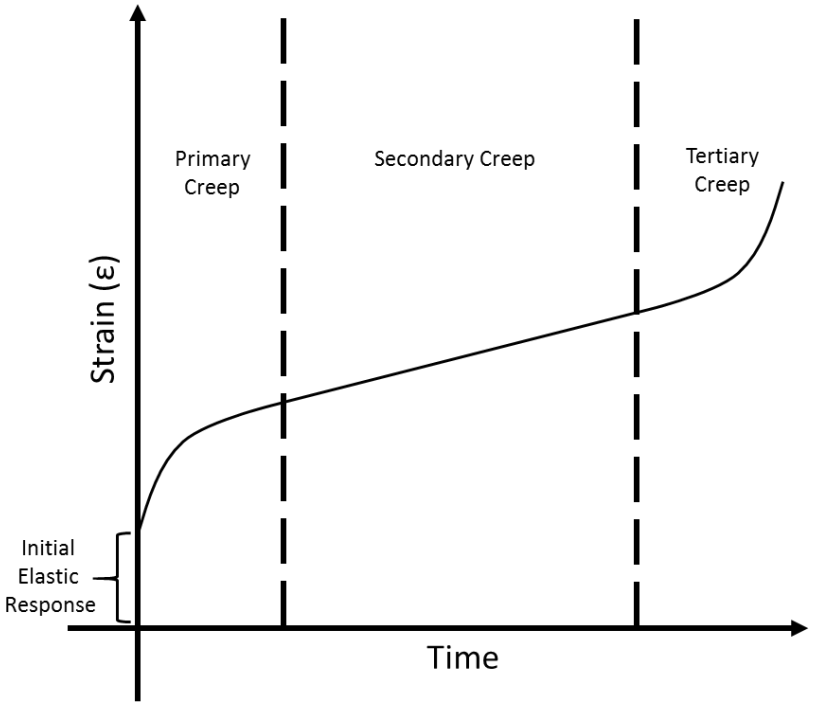

Figure 5: Schematic of an idealized creep curve for a material under a constant applied load (After Jaeger et al., 2007).

Actual creep rates of in situ rock salt are dependent on the stress regime, temperature, depth, and impurities in the rock salt among others factors (Swift and Reddish, 2005; Wittke, 2014). Ambient humidity may be an additional factor having a seasonal effect on the creep rates of in situ rock salt (Sambeek, 2012). Often mathematical or rheological models are used to describe the mechanical behaviors of rock salt, which can then be incorporated into numerical finite element models for stability analyses, subsidence predictions and other studies. Understanding the creep behavior of in situ rock salt at a given location is important for designing mines so that collapses and extreme subsidence can be avoided.

2.3 Subsidence associated with subsurface excavations

In this section, factors controlling surface subsidence associated with underground excavations are discussed. The primary focus of this thesis and, therefore, this section, is on room and pillar mining; however, many of the same principles apply to solution mining cavities as well.

Surface subsidence is expected to result from underground mining as a consequence of internal deformation of the pillars and walls supporting the ceiling (e.g., Lee and Abel, 1983; Kratzsch, 1983). Subsidence is a complex process involving a large number of factors contributing to the spatial extent and magnitude of displacements observed at the surface. Such factors include the dimensions and geometry of the mined salt layer, depth of mining, dimensions of the excavation, rate of advance, backfilling, properties of overlying and underlying strata, presence of joints and faults, variations in surface topography, interactions of groundwater with the mine workings, and discontinuities in the overburden (e.g., voids or facies changes) (Sambeek, 2000; Lee and Abel, 1983).

Surface deformation associated with mining consists of both vertical and horizontal displacements (Sambeek, 2000; Lee and Abel, 1983; Kratzsch, 1983). Generally, maximum vertical subsidence occurs towards the center of a mined area and gradually decreases towards the edges of the mining region, with lateral variations in vertical displacements resulting in changes to the surface slope (Sambeek, 2000; Kratzsch, 1983). For a simple scenario, (*Figure 6*) predicted horizontal displacements are zero at the point that experiences maximum vertical subsidence, and horizontal strains are tensile and compressive towards the edges and center of the subsidence basin respectively (*Figure 6*) (Sambeek, 2000; Kratzsch, 1983).

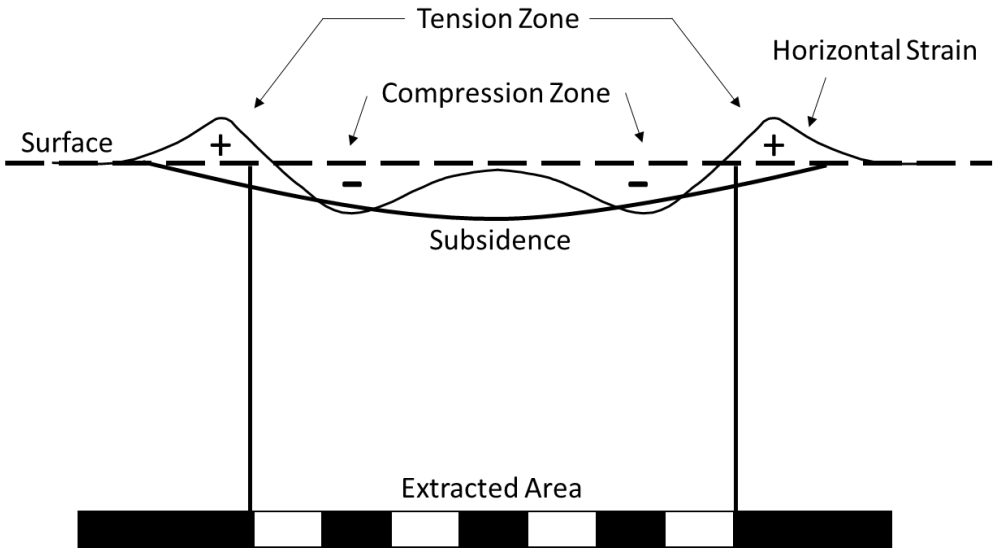

Figure 6: Idealized subsidence basin from room and pillar mining of a single layer (Adapted from Akzo Hampton Corners subsidence report, 1995).

Subsidence observed at the surface is an expression of the cumulative deformation from all of the excavations in the subsurface, controlled by the span (spatial extent) of the mine dictates how much vertical subsidence occurs at the surface given the extraction ratio, depth, and properties of the overburden such as composition of strata, structural integrity (e.g., joint and fractures) of units, thickness of units, and strength of individual units (Sambeek, 2000; Lee and

Abel, 1983). Sambeek, 2000, suggests that the amount of observed subsidence is correlated with the quantities of shale, limestone, and sandstone in the overburden. Namely, less subsidence is observed with greater quantities of shale and limestone, whereas more subsidence is observed when more sandstones are present (Sambeek, 2000).

The final amount of subsidence resulting from salt mining can take up to a century to complete depending on the rate at which the salt pillars shorten through steady state creep (Kratzsch, 1983). The maximum achievable subsidence at the surface can be partially offset by backfilling of mines or by intentional (or accidental) flooding of the mine with water (e.g., Retsof) (Berest et al., 2004).

Subsidence can cause damage to overlying structures and can be used as an indicator of mine stability, hence the spatial extent and magnitude of subsidence is often monitored by the mine or other agencies. For salt, the long time scale of potential subsidence could require mine operators to commit expensive to long term monitoring and maintenance of subsidence related damages. Differential vertical strains, changes to surface slope, and horizontal strains all can have adverse effects on buildings, roads, agricultural fields, hydrological systems, surface drainage, and property values (Sambeek, 2000; Lee and Abel, 1983). The development of fractures associated with subsidence can alter surface and groundwater flow as well. These changes in the subsurface water networks can pose a threat to the mine, as fracture networks can allow water infiltration into the mine (Lee and Abel, 1983). Damage to buildings ranges on a scale from very slight (cracked plaster) to very severe (broken windows/buckling roof and walls) depending on the magnitude of subsidence (Lee and Abel, 1983).

2.4 Case studies of salt mine subsidence and collapse

2.4.1 Retsof, New York

The Retsof mine in western New York State was the largest salt mine in the US and operated for 100 years prior to closing. Catastrophic ceiling failure and subsequent water suffusion occurred in 1993, filling the entire mine with water over a period of two years. Two large sinkholes formed over caved in rooms, local wells ran dry, gas seeps were detected in ground water, widespread surface subsidence occurred over most of the southern section of the mine, and nearby roads and a bridge were damaged (Nieto and Young, 1998; Yager et al, 2001).

During 1993, prior to the eventual collapse, anomalously high room convergence rates were detected in mine rooms 2 Yard South and 11 Yard West of the Retsof Mine – potentially a sign of the tertiary creep described in Section 2.2. The company had used traditional room and pillar mining methods with an extraction ratio of about 67%, which did not leave sufficient material to prevent further convergence and weakening of the mine ceiling. To mitigate room convergence the yield pillar technique (described in Section 2.1.2) with a much higher extraction ratio (up to 90%) was used. The yield pillar method is designed to minimize room closure by forming a stress arch in the overlying strata between much stronger abutments (Yager et al., 2001; Yuvaz, 2001). However, potentially due to discontinuities in the overburden that were later discovered (a fracture system and brine and gas pool), the overlying strata were unable to support this load (Whyatt and Varley, undated). The roof collapsed, forming a rubble zone that propagated into the overlying bedrock and reaching the Onondaga-Bertie contact (Yager et al, 2001). As a consequence, the smaller saline bedrock aquifers contained near the Onondaga-Bertie contact leaked into the collapsed mine rooms at a rate of about 5,500 gallons per minute. Attempts to mitigate the flow of water failed and eventually the rubble zone propagated past the

Onondaga formation into the rest of the overlying strata and glacial sediments. The lower glacial valley aquifers residing in the Genesee Valley contributed to the flooding of the mine and increased water inflow rates to about 18,000 gallons per minute. Over a period of two and a half years the entire Retsof Mine was flooded with water and the mine officially shut down in 1995 (Yager et al, 2001; Yager, 2013).

2.4.2 Wieliczka, Poland

The Wieliczka Mine is more than 700 years old and extends to about 300 meters below the surface with a complex network of more than 2000 rooms throughout the upper and lower salt deposits (Perski et al., 2009). The geologic setting at Wieliczka is complex consisting of a thick sequence of tectonically deformed salt deposits categorized into two groups, the upper brecciated evaporate deposits and the lower layered deposits (e.g., Perski et al. 2009; Brudnik et al., 2010). The upper deposits consist of large rock salt blocks which have been mined out, forming the large rooms in the upper section of the mine. The upper deposits are overlain by clay-gypsum deposits and sedimentary layers approximately 40 - 50 meters thick. The lower deposits are interlayered with siltstone, sandstone, and claystone and the rock salt layers are more variable in thickness and composition (Perski et al, 2009; Brudnik et al., 2010). Highly fractured water bearing beds are located north of the salt deposits.

The current regime of subsidence associated with the Wieliczka Mine is complex due to the long history of mining activity. Throughout its history, the Wieliczka Mine has experienced episodes of enhanced subsidence due to water inflows which deteriorated parts of the mine (Brudnik et al., 2010) eventually leading to collapse of the largest room in 1974 (Perski et al., 2009). Geodetic measurements of subsidence have been made in the region since 1925, with

peak subsidence rates of 7.2 cm/yr observed in 1962 which decreased to 2.2 cm/yr by 2009. More recently Persistent Scatterer InSAR (PS InSAR, Perski et al., 2009) observations found maximum current subsidence rates of approximately 2.3 cm/yr at Wieliczka.

2.4.3 Varangeville, France

The Varangeville Mine in Lorraine, France, which is currently still active, experienced roof collapse on October 30, 1873. Collapse of the mine occurred around the shaft in the Saint-Maximilien panel with a number of resulting fatalities. The collapse caused the formation of two sets of concentric rings at the surface with radii of 80 and 160 meters. Cracks developed at the outer ring and folds developed at the inner ring indicating tensile and compressive strains respectively, and the ground within the inner ring subsided evenly by about 3.3 meters (Bérest et al., 2007). Prior to the collapse, the ground surface was estimated to have subsided a few decimeters, although the length of time subsidence occurred over was not specified.

At the Maximilien panel, the mine utilized large extraction ratios (over 82%) leaving behind 6 × 6 meter wide pillars with rooms about 8 – 9 meters wide while a large central pillar about 29 × 40 meters was left around the mine shaft. The mine panel underlies about 156 meters of overburden consisting mainly of marls with mixed amount of carbonaceous content, while salt in the region occur in 11 layers that are separated by marl layers approximately 0.5 – 3 meters thick. The Maximilien panel was in the bottom most layer of salt which is about 20 meters thick and underlain by an approximately 25 meter thick layer of marl (Bérest et al., 2007).

Preceding the collapse, vertical fractures were found on a number of the pillars, but there was minimal indication of salt creep. The lack of flow in the pillars is partly accounted for by the large extraction ratios used in developing the mine. Due to the thin pillars, much of the load

from the overburden was transferred to the mine abutments in a way that is similar to what is expected during use of the yield pillar method (Bérest et al., 2007). Additionally, the use of water for assisting in salt mining caused exposure of the underlying marls to under saturated water resulting in oxidation of the marls with a significant reduction in strength. Consequently, the pillars punched into the underlying marls assisting in the transference of stress to the abutments (Bérest et al., 2007).

Following the collapse, minimal damage was observed in mine workings overlying the area of the collapsed panel and in the center shaft. Because of the lack of damage, the collapse is thought to have occurred as the downward movement of a single large block of rock centered on the center pillar and contained within the inner circle observed on the surface (Bérest et al., 2007). It is suggested that large shear stresses developed on the edges of the panel as a consequence of the transfer of stress to the abutments, ultimately resulting in failure of the roof in a ring around the center pillar (Bérest et al., 2007).

CHAPTER 3

INTRODUCTION TO INSAR

3.1 Overview of InSAR

Interferometric Synthetic Aperture Radar (InSAR) is a technique used to measure topography or ground displacements between consecutive data acquisitions with centimeter to millimeter scale precision (Burgmann et al., 2000; Rosen et al., 2000; Massonnet and Feigl, 1998). InSAR utilizes electromagnetic waves at the microwave to radio frequencies emitted from an antenna attached to either ground-based or airborne platforms, or satellites. The antenna illuminates a swath on the ground surface and the phase and amplitude of the reflections are recorded back at the antenna. A single data acquisition yields a synthetic aperture radar (SAR) image containing both amplitude and phase information of the radar echoes. With multiple SAR images acquired at successive times, changes in phase between time periods can be used to construct a history of ground displacements (Rosen et al., 2000).

InSAR differs from geodetic techniques such as GPS and leveling in that it provides areal coverage of the ground surface on the order of tens to thousands of square kilometers, with spatial resolutions on order of 1 – 30 meters per pixel (Burgmann et al, 2000). Another distinction is that InSAR provides measurements of changes to the radar path along the line of sight (LOS) between the satellite and the ground, so that observations are a vector combination of vertical and horizontal ground displacements (Rosen et al., 2000; Burgmann et al., 2000). The temporal resolution of InSAR is often on the order of weeks to months, much less than the potential resolution provided by continuous or even campaign GPS. However, in remote or otherwise hard to access areas, InSAR can provide coverage that would be prohibitively

expensive with ground-based observations. Due to the high spatial resolution, and large areal coverage, space-based InSAR serves as a good exploratory tool for finding undocumented signals.

The applications of InSAR have been expanding since the 1990's including significant contributions to volcanology, active tectonics (e.g., earthquake deformation), glaciology, and geotechnical analyses (e.g., land subsidence) (Massonnet and Feigl, 1998), and more recently including developments in biomass estimates (e.g., Prush and Lohman, 2014), soil moisture mapping (e.g., Nolan et al., 2003), snow cover (e.g., Guneriussen, 2001), and hydrology (e.g., Farr et al., 2015). Specific examples include monitoring of volcano deformation for the purpose of studying magma migration and estimating magma chamber locations and volumes through model inversions (e.g., Yun et al., 2006), improved earthquake locations through fault slip inversions of measured deformation fields (e.g., Lohman and Simons, 2005), or characterization of land subsidence in Southern California from extensive groundwater pumping (e.g., Farr et al., 2015). InSAR often has been used to characterize the temporal and spatial features of mining induced subsidence signals, and, has been used to infer, to a limited extent, the properties of the mine workings (e.g., Platterner et al., 2010; Perski et al., 2009; Raucoules et al., 2003; Chengsheng et al., 2010; Carnec and Delacourt, 2000; and Hongdong et al., 2015).

The number of satellites with SAR capabilities used for scientific purposes is increasing, as is data availability (*Figure 7*). The earliest satellites that were widely used for SAR interferometry such as ERS 1-2 or JERS-1 were not specifically designed for that purpose. Orbital parameters of the satellites were not controlled to a high level of accuracy and the revisit periods (time for satellite to pass over the same area) were long (on order of 35 – 48 days). The temporal resolution of space based SAR systems has increased significantly in recent years with

satellite deployments such as TerraSAR-X, Cosmo-SkyMed, Sentinel, and ALOS-2 which have revisit times on order of 8-11 days. The future NASA-ISRO SAR mission (NISAR), run jointly between the National Aeronautics and Space Administration (NASA) and the Indian Space Research Organization (ISRO) is expected to significantly increase the areal coverage for InSAR data acquisitions and is anticipated to increase the accessibility of SAR products to the scientific community.

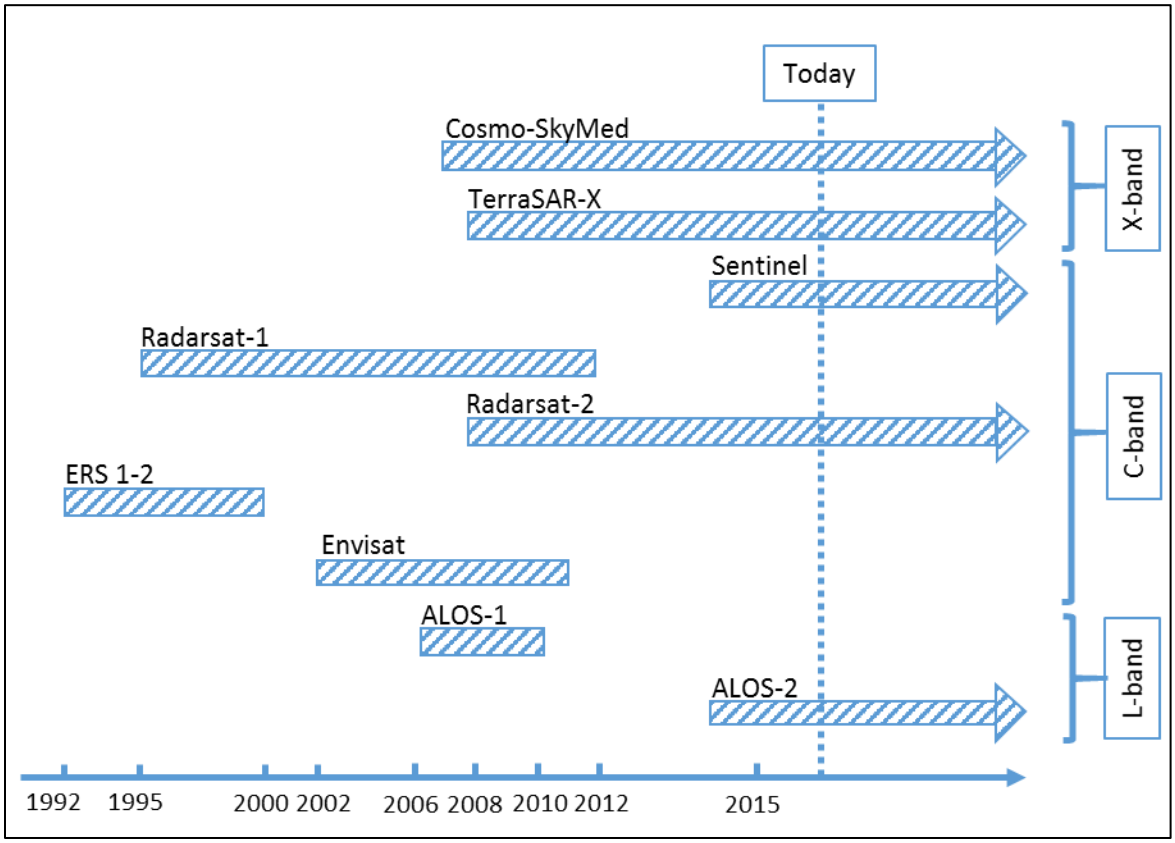

Figure 7: Timeline of InSAR capable satellites with repeat pass cycles (Adapted from the European Space Agency).

3.2 Principles of InSAR

Repeat pass InSAR uses two independent measurements of the phase from reflected SAR echoes off the ground surface. The measurements are obtained at different times, and typically from different positions, where the spatial separation between observation points, $\vec{\mathrm{B}}$, is known as the baseline (*Figure 8*). Differencing of the phase measurements yields the interferometric phase, which is related to the baseline and the range distance to the ground target, and is approximately given by

$$\phi = -\frac{4\pi}{\lambda}\left[\left(\vec{B}\cdot\widehat{l_1}\right) - \left(\vec{D}\cdot\widehat{l_1}\right)\right], \tag{3.1}$$

where $\widehat{l_1}$ is the unit vector in the range direction of the first acquisition and $\vec{D}$ is the ground surface displacement vector (e.g., Burgmann et al., 2000). Non-zero baselines introduce a component in the interferometric phase that is related to topography. As the baseline between antennae increases, the component becomes greater; hence, for longer baselines, a significant component of the interferometric phase can be attributed to topography (e.g., Burgmann et al., 2000). Conversely, if the baseline is close to zero, the topographic contributions are negligible. To obtain the interferometric phase component attributed to surface displacements, the topographic components are typically removed with a synthetic interferogram generated from a DEM and assuming the antennae positions. Once the interferogram is corrected for topography, the resultant interferometric phase theoretically consists only of displacements from the ground surface, however, there are usually a number of noise terms contributing to the interferometric phase, including ionospheric and tropospheric phase effects (e.g., Burgmann, 2000).

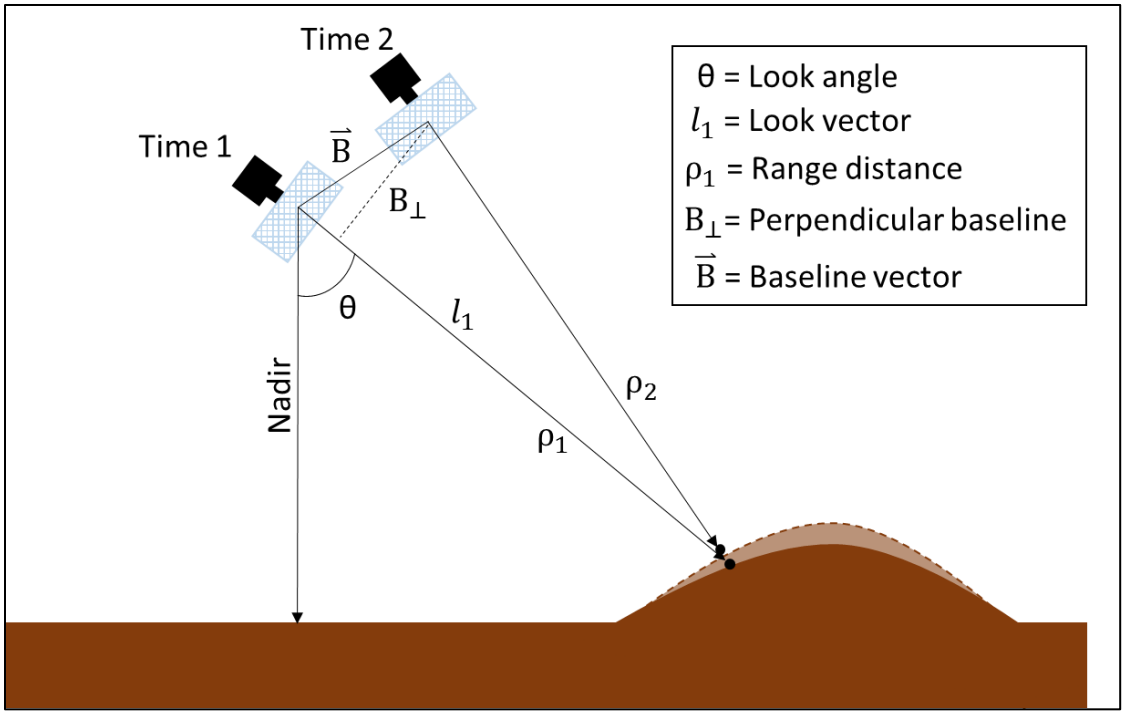

Figure 8: Schematic of the geometry for repeat pass satellite based InSAR measurements of ground deformation.

The interferometric phase represents LOS measurements of the ground displacements in terms of the fraction of a wavelength, not as absolute distances. In other words, they are only known to modulo 2π. To obtain absolute measurements of LOS ground displacements, phase unwrapping must be performed. Phase unwrapping is a method for intelligently summing interferometric phase fringes along 2π discontinuities, either in 1- or 2-D, in order to generate an absolute deformation map (Burgmann, 2000). The phase unwrapping method used in this thesis is the Statistical-cost Network-flow Algorithm for Phase Unwrapping (SNAPHU), (Chen and Zebker, 2002), which unwraps the phase to generate the most likely solution given the input data.

CHAPTER 4

PROCESSING METHODS

4.1 Introduction

The processing scheme used in this study is a combination of Persistent Scatterers (PS) (e.g., Colesanti et al., 2003, Hooper et al., 2007) and Small Baseline Subsets (SBAS) (e.g., Berardino et al., 2002) algorithms and builds on a combination of software including ROI_PAC (Rosen et al., 2000) and SNAPHU (Chen and Zebker, 2002). The combination of SBAS and PS techniques (e.g., Hooper et al., 2004) allows us to optimize the coherence of individual interferograms (SBAS) and focus only on the high-quality pixels (PS). This is particularly advantageous in this study, since we are limited to a relatively small number of radar image acquisitions that usually contain significant levels of noise, some with contributions from snow cover.

4.2 SBAS Processing

For n SAR scenes, d_1, d_2, …, d_n, acquired over the same region, we have $\frac{n!}{2!(n-2)!}$ possible date pair combinations, (d_i, d_j), assuming no repetition of combinations. By convention we choose to construct all interferograms with the earlier date first i.e., (d_i, d_j) where $i < j$ and the time intervals between the master and secondary images are given by $d_j - d_i$. A master scene, d_m, is chosen from a given set, such that the perpendicular baseline of the secondary scenes with respect to the master are minimized. Because of the limited number of acquisitions in this case (~10), we find that it is useful to make interferograms spanning all pairs of dates and remove selected pairs over iterations after phase unwrapping.

4.3 Generation of Interferograms

We form Single Look Complex images (SLCs) for each individual acquisition that contain full resolution complex phase and amplitude information, using ROI_PAC. All of the secondary SLCs are co-registered to the master SLC using ROI_PAC software, based on a mapping obtained from cross-correlations between the master and secondary SLC amplitude images.

To generate interferograms, (d_i, d_j), by calculating the interferometric phase, ϕ, for each date pair, we multiply the complex phase of the full resolution master SLC by the complex conjugate of the co-registered secondary SLC on a pixel by pixel basis. The resulting images contain information regarding potential surface deformation (ϕ_d) and topography (ϕ_t), contributions from orbital errors (ϕ_o), and path delays due to variations in the refractive index between the satellite and the ground (ϕ_α) typically due to variations in tropospheric moisture content. The total interferometric phase is thus given by

$$\phi_{tot} = \phi_d + \phi_t + \phi_o + \phi_\alpha + \phi_c \qquad (3.1)$$

where ϕ_c are the contributions to phase from thermal noise and co-registration errors (Burgmann et al., 2000). In cases where we have many interferograms, many of the terms can be approximated or modeled due to their differing temporal and spatial characteristics.

4.4 Estimating Phase Stability

The goal of persistent scatterer interferometry (e.g., Colesanti et al., 2003, Hooper et al., 2007) is to identify pixels with spatially and temporally stable phase characteristics. Such pixels tend to be similar to their neighbors over time, so we select them by comparing each pixel to the average of its neighbors in each interferograms with the following approach. We filter the real and imaginary components of the phase with a 20 by 20 pixel Gaussian filter to obtain a smoothed average of the spatial component of the phase. Differencing the filtered phase from the original unfiltered phase through multiplication of the complex conjugate yields a residual,

$$\varphi_{\mathrm{res}} = \arg(\mathrm{e}^{i\varphi} * \overline{\mathrm{e}^{\imath\varphi_{\mathrm{f}}}}), \tag{3.2}$$

which characterizes the variation of the noise, where $e^{i\varphi}$ is the complex phase and $\overline{e^{\imath\varphi_f}}$ is the complex conjugate of the filtered complex phase, $\overline{e^{\imath\varphi_f}} = \cos(\varphi_f) - i\sin(\varphi_f)$. A residual is calculated for each interferogram, and the variance of the complex phase, γ, is given by

$$\gamma = -2\ln\left|\frac{1}{\mathrm{n}}\sum_{\mathrm{k}=1}^{\mathrm{n}} \mathrm{e}^{i(\varphi_{\mathrm{res,k}})}\right|, \tag{3.3}$$

where n is the number of flattened, wrapped interferograms. This approach is similar to that used in Hooper et al., 2004.

4.5 Spatial Averaging and Phase Unwrapping

We spatially average the interferograms (down-look) based on a weighting of the pixels derived from an estimate of the phase variability for each pixel (Equation 3.3). Typically, in PS based methods, pixels with stable phase properties are determined, and sparse or 3D phase unwrapping algorithms are applied to the full subset of selected pixels (e.g., Hooper et al., 2007). By down-looking the phase we can incorporate the benefits of PS pixel selection and reduce image speckle while applying commonly used 2D phase unwrapping algorithms.

Let r_l and a_l be the downsizing factors in range and azimuth respectively. Then for each interferogram, we spatially average over $a_l \times r_l$ pixel area, with the contribution from each pixel weighted by the reciprocal of γ such that

$$\phi_k = \frac{1}{a_l r_l} \sum_{i=1}^{a_l} \sum_{j=1}^{r_l} \varphi_{f,i,j,k} w_{i,j,k} \tag{3.4}$$

where ϕ_k is the phase for a given down-looked pixel, k, and $w_{i,j,k} = \frac{1}{\gamma_{i,j,k}}$. The down-looked interferograms, ϕ_i, have dimensions $x_l = \left\lceil \frac{x}{r_l} \right\rceil$ and $y_l = \left\lceil \frac{y}{a_l} \right\rceil$ for the range and azimuth directions respectively where $\lceil \rceil$ is the floor operator.

We unwrap the down-looked interferometric phase with SNAPHU (Chen and Zebker, 2002). We implement the tile mode, which reduces the computational cost and time to unwrap large images without any significant changes in accuracy.

4.6 LOS Deformation Time Series

Interferograms often contain a long spatial scale signal due to errors in orbital corrections or tropospheric phase delays, neither of which are of interest in studies of local deformation sources such as those associated with a salt mine. To account for these contributions, we invert for a quadratic phase ramp for each interferogram and subtract the fit from the flattened, unwrapped phase maps. Following the ramp removal, we invert for LOS cumulative deformation at each date (see below), and subsequently invert for the average secular LOS deformation rates with a generalized least squares solution.

We invert for cumulative LOS deformation at each date from the selected unwrapped interferograms using a least squares inversion based on the available set (tree) of interferograms. We have Gm = d, where G is the design matrix relating actual signal present on each date (ground deformation path delays) to the interferograms, m is the cumulative deformation at each of the N dates (model parameters), and d is the data from M interferograms. Each row of the M×N design matrix, G, contains -1 in the position of the secondary date, 1 for the master date, and zeros everywhere else, where the columns denote dates and the rows indicate interferograms. To enforce a zero deformation constraint on the master date, we add a row of zeros with a 1 at the d_m position and a "pseudo-data" value of zero to our data vector. For instance, if we have d interferograms (d_1, d_2), (d_1, d_3), (d_2, d_3), and (d_3, d_4), where d_2 is the master date, then

$$G = \begin{bmatrix} -1 & 1 & 0 & 0 \\ -1 & 0 & 1 & 0 \\ 0 & -1 & 1 & 0 \\ 0 & 0 & -1 & 1 \\ 0 & 1 & 0 & 0 \end{bmatrix}. \quad (3.1)$$

Note that the addition of the final row makes the problem an overdetermined system.

It is optimal to construct interferograms such that the set is continuous through time, however this is not always possible. Often, there are dates that must be excluded in the time series inversion because of poor interferogram quality. This can cause gaps in the design matrix. For example, if

$$G = \begin{bmatrix} -1 & 1 & 0 & 0 & 0 \\ 0 & 0 & 0 & -1 & 1 \end{bmatrix}, \tag{3.2}$$

then the date associated with the third column, d_3, is unresolved and the interferogram set is discontinuous since there is no interferogram spanning the missing time interval. We address this problem by, again, adding constraints to the problem that minimize the difference in rate during the unconstrained time periods and the constrained time periods. This is different than what would result if we used, say, a damped least squares approach, which would result in the unconstrained time intervals having a rate of zero.

For small sets of interferograms such as that shown in Equation 3.2, it is easy to determine which time periods are unconstrained. However, for larger sets this can become unwieldy. To automate the approach, we use singular value decomposition (SVD) to determine the rank of our design matrix and the time periods that lack constraint. We decompose the design matrix, $G = USV^T$, where U is an N×N matrix of eigenvectors which span the data space, V is an M×M matrix which spans the model space, and S is an N×M diagonal matrix containing the singular values of the design matrix (e.g., Menke, 1989). The rank, p, of the matrix is given by the number of non-zero singular values and is used to truncate the matrices from the SVD decomposition. The generalized solution for the SVD method is then given by $G^{-g} = V_p S_p^{-1} U_p^T$ where V_p, S_p, and U_p are respectively the truncated versions of V, S, and U (Menke, 1989).

We define "poorly-resolved" model parameters as those where the diagonal of the model resolution matrix, R_m, of the truncated SVD decomposition are small. Perfectly resolved dates will have a resolution of unity. The model resolution matrix is given by

$$R_m = \left[V_p S_p^{-1} U_p^T\right]\left[U_p S_p V_p^T\right], \tag{3.3}$$

(e.g., Menke, 1989). For dates where the diagonal of R_m is less than a threshold value, h, we constrain that date to fall on the mean fit to the remaining dates.

Fit quality for a given pixel is estimated by the standard deviation of the model residuals, σ_r, where

$$\sigma_r = \sqrt{\frac{(r-\bar{r})^2}{n-1}}, \tag{3.4}$$

$r = G_{svd}m - d$ are the residuals, $\bar{r}$ is the mean of the residuals for each pixel, and n is the number of dates. We solve for the LOS average deformation rates in a least squares sense, where

$$Gr_{los} = m, \tag{3.5}$$

and

$$G = \begin{bmatrix} 1 & t_1 \\ 1 & t_2 \\ 1 & t_3 \\ \vdots & \vdots \\ 1 & t_n \end{bmatrix}. \tag{3.6}$$

We have $\mathrm{r_{los}} = \mathrm{m}[\mathrm{G^T G}]^{-1}\mathrm{G^T}$, and a measure of the fit quality is given by $\sigma_{\mathrm{r_{los}}} = \sqrt{\frac{(\delta - \bar{\delta})^2}{\mathrm{n}-1}}$ where $\delta = \mathrm{Gr_{los}} - \mathrm{m}$. Both σ_{r} and $\sigma_{\mathrm{r_{los}}}$ can be used to mask pixels which fit the model inversions poorly in the final average rate map.

CHAPTER 5

DATA AND RESULTS

5.1 Introduction

In this Chapter, I investigate salt mine subsidence in western New York using InSAR time series generated from the techniques discussed in Chapter 4. I processed all available ALOS-1 data for the area (Table 1, Figure 9). Multiple overlapping satellite tracks provide complete coverage across the entire region (Figure 9) with increased coverage in the overlapping portion of the swaths. Of the locations of salt mining activity, the American Rock Salt (ARS) Mine is the only area associated with InSAR observations of subsidence. I was able to assess the accuracy of the InSAR time series results for the site by comparing against leveling data provided by the American Rock Salt Company.

In vegetated terrains and agricultural lands such as those that cover much of western NY, interferograms are often decorrelated due to volumetric scattering, land surface change, and variations in soil moisture content (e.g., Zebker and Villasenor, 1992). Variations in atmospheric water vapor and snow on the ground surface are other potential noise sources that can greatly alter the interferometric phase. The L-band (23.6 cm wavelength) observations such as those from the PALSAR instrument on the Japanese ALOS-1 satellite perform relatively well in vegetated terrain when compared to shorter wavelength (i.e., C- and X-band) instruments (e.g., Sandwell et al., 2008).

Effects on interferograms due to temporal variations of the ionosphere or water vapor in the troposphere can be assumed to average to zero over time, because these properties change rapidly (time scales of minutes to hours) compared with the repeat time of the available SAR

satellites. However, the strength of remaining atmospheric signal in a particular InSAR time series will depend on the number of images available and how well distributed they are in time. Precisions of a few mm/yr can be obtained in cases where there are many images and few other sources of decorrelation (e.g., Finnegan et al., 2008).

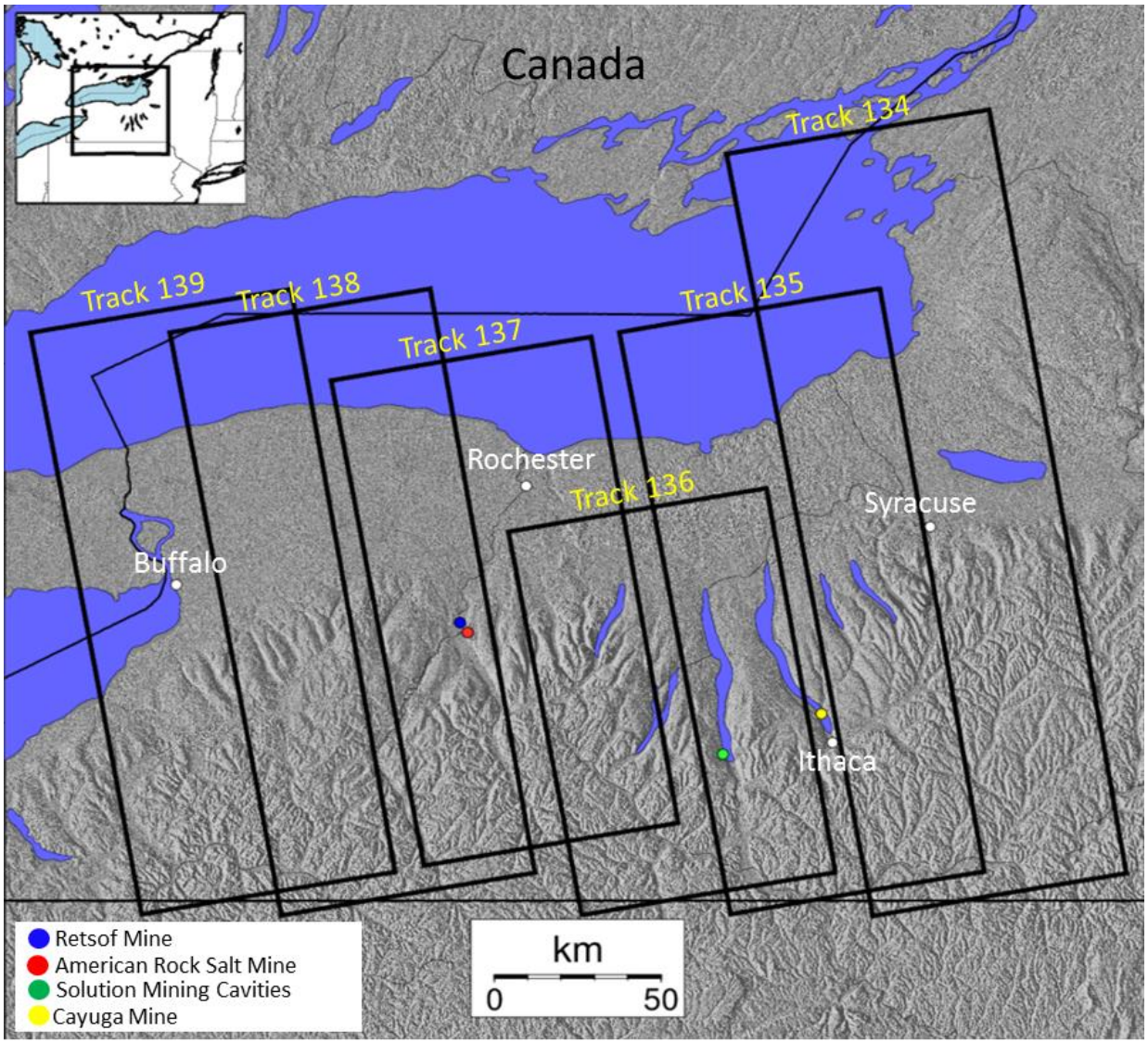

Figure 9: Map of western NY with InSAR satellite coverage used for this study.

Table 1: ALOS-1 data across western NY for satellite tracks shown in Figure 9. Perpendicular baseline and time between consecutive dates are given with respect to the master date.

Date	$B_{\perp}$ (m)	Time (days)	Track
Jan-08-2007	0	0	138
May-26-2007	1939	138	138
Oct-11-2007	3245	276	138
Jan-11-2008	3884	368	138
May-28-2008	4870	506	138
Jul-13-2008	1466	552	138
Mar-03-2010	3378	1150	138
Apr-18-2010	3647	1196	138
Jun-03-2010	3810	1242	138
Jul-19-2010	3884	1288	138
Sep-03-2010	4272	1334	138
Dec-04-2010	4559	1426	138
Jan-19-2011	5077	1472	138
Mar-06-2011	5739	1518	138
Dec-22-2006	2634	-1196	137
Jun-26-2008	1393	-644	137
Apr-01-2010	0	0	137
Aug-17-2010	-780	138	137
Nov-17-2010	-822	230	137
Feb-17-2011	-2226	322	137
Sep-24-2007	472	-920	137
Aug-14-2009	1788	-230	137
Jul-02-2010	-612	92	137
Oct-02-2010	-1087	184	137
Jan-02-2011	-1495	276	137
Dec-05-2006	-1690	-136	136
Dec-08-2007	0	0	136
Jul-28-2009	-2349	598	136
Mar-15-2010	-36	828	136
Apr-30-2010	117	874	136
Jun-15-2010	129	920	136
Sep-15-2010	532	1012	136
Oct-31-2010	959	1058	136
Dec-16-2010	1130	1104	136
Jan-31-2011	1800	1150	136

Table 1 (Continued)

Date	$B_{\perp}$ (m)	Time (days)	Track
Dec-13-2007	-425	-1012	139
Apr-29-2008	1199	-874	139
Jun-17-2009	-2745	-460	139
Sep-17-2009	-2505	-368	139
Jun-20-2010	-364	-92	139
Aug-05-2010	-72	-46	139
Sep-20-2010	0	0	139
Nov-05-2010	-30	46	139
Dec-21-2010	590	92	139
Feb-05-2011	1209	138	139
Aug-21-2007	-790	-1012	135
May-23-2008	1213	-736	135
Jul-08-2008	-2079	-690	135
Jul-11-2009	-2210	-322	135
Jan-11-2010	-1019	-138	135
Feb-26-2010	-303	-92	135
May-29-2010	0	0	135
Jul-14-2010	115	46	135
Aug-29-2010	567	92	135
Oct-14-2010	878	138	135
Nov-29-2010	934	184	135
Jan-14-2011	1480	230	135
Sep-19-2007	977	-736	134
Dec-20-2007	1565	-644	134
Sep-21-2008	-2332	-368	134
Dec-22-2008	-1968	-276	134
Sep-24-2009	0	0	134
Dec-25-2009	652	92	134
Mar-27-2010	1674	184	134
May-12-2010	1683	230	134
Jun-27-2010	1756	276	134
Aug-12-2010	2242	322	134
Nov-12-2010	2131	414	134
Dec-28-2010	2953	460	134
Feb-12-2011	3714	506	134

In this study, we also must consider the impact of snow since the region is known to frequently have large accumulations of snow on the ground surface and experiences severe snowstorms. We confirm that significant InSAR phase delays associated with snow by correlating individual interferograms with independent models of Snow Water Equivalence (SWE) from the SNOw Data Assimilation System (SNODAS) by the NOAA National Weather Service's Hydrologic Remote Sensing Center (NOHRSC). For the purposes of this work, we removed interferograms that were associated with large snow events from the time series.

5.2 Snow

Snow cover can greatly degrade the quality and/or bias the interferometric phase of interferograms constructed with SAR images obtained during winter months (e.g., Guneriussen et al., 2001). Since it is difficult to determine the extent of snow cover at a given time, care must be taken when observing deformation signals in interferograms potentially containing snow. Recognizing and removing interferograms with poor coherence can be done with relative ease, however, interferograms with snow cover can remain coherent while containing significant phase changes that can bias displacement estimates. The effects of snow on anthropogenic signals is potentially reduced since the length scales of anthropogenic signals are often much smaller than signals from snow. Nevertheless, to prevent degradation of time series accuracy, interferograms containing snow were removed during construction of the deformation time series (e.g., *Figure 17*).

Interferogram coherency depends on spatial and temporal baselines in addition to variations in the scattering properties of the surface between scenes. Scenes which contain phase and amplitude information from similar scatterers on the surface generally produce more

coherent interferograms (e.g., Zebker and Villasenor, 1992). As the spatial baseline increases between scene acquisitions, the viewing geometry is altered and the recorded phase and amplitude corresponding to locations on the ground may be significantly different either due to different interactions of the electromagnetic radiation with surface scatterers or interactions with different scatterers. Additionally, as with greater time between scenes, the likelihood that the ground surface has changed increases leading to a higher likelihood of producing decorrelated interferograms.

The presence of snow cover can greatly alter the scattering properties of the ground surface. If snow is present in one or more of the scenes used in making an interferogram, then the measured phase is often significantly different between scenes resulting in decorrelation. However, the coherence of interferograms has been related to the moisture content of snow cover. Higher moisture content in snow (wet snow) significantly changes the scattering properties of the surface resulting in decorrelation, while when the moisture content of the snow is low (dry snow), the electromagnetic radiation penetrates the snow and reflects off the ground surface maintaining coherence (e.g., Guneriussen et al., 2001). In the case of dry snow, significant phase changes result due to refraction of electromagnetic waves at the snow/air interface, and from variations of properties within the snowpack (e.g., *Figure 10*). Researchers have related phase changes to the snow permittivity, antennae wavelength, satellite incidence angle, and thickness of the snowpack (e.g., Gueriussen et al., 2001), whereas other models (e.g., Phan et al., 2014) take into account volume scattering and a greater number of properties of the snow pack.

We use independent datasets of SWE from SNODAS by NOHRSC to confirm that observed phase changes in interferograms correspond to snow cover. Examples of

interferograms containing snow that correspond well to the SWE data show that external datasets can potentially be incorporated into InSAR processing for snow-phase corrections. Conversely, it is suggested that the accuracy of SWE models can be improved through the integration of SAR data (e.g., Guneriussen et al., 2001). The study of snow and SAR data requires continued development before such goals can be achieved. For this thesis, we simply document instances of phase changes in interferograms corresponding to snow cover for InSAR tracks shown in Figure 9 which are in good agreement with the SNODAS SWE models.

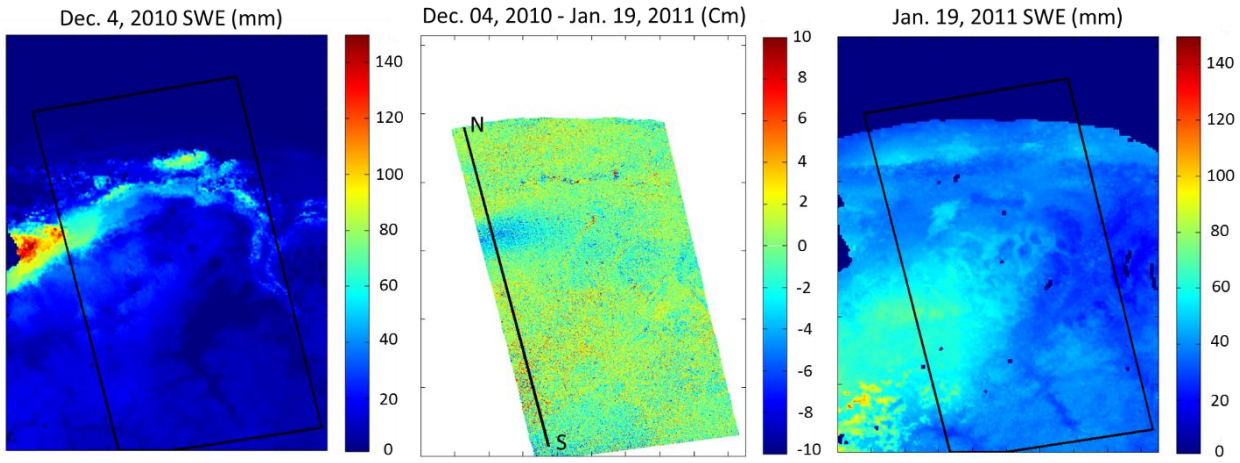

Figure 10: Interferometric phase changes associated with snow for the dates Dec. 04, 2010 – Jan. 18, 2011 from Track 138 (center), and SNODAS SWE models corresponding to each date (left and right).

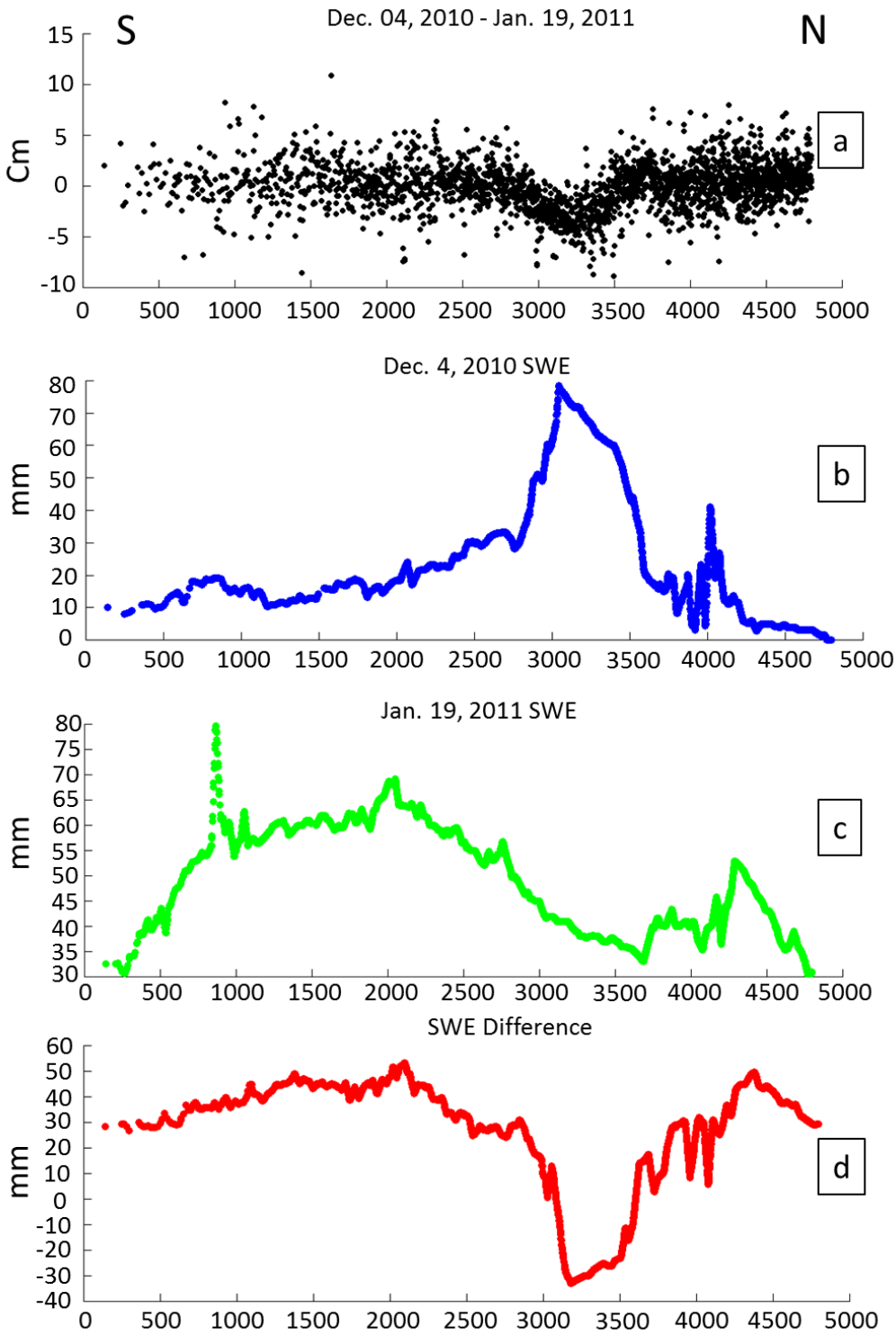

Figure 11: Profiles of the interferogram from Dec. 04, 2010 – Jan. 19, 2011 (a) and of the corresponding SWE models (b and c) for each date, and the difference of the SWE models (Jan. 19, 2011 minus Dec. 04, 2010) (d). Location of the profiles is shown in Figure 10.

The effects of snow are clearly shown in Figure 10 for an interferogram constructed using two date acquisitions (Dec. 04, 2010 – Jan. 18, 2011) acquired during winter months. Significant phase delays corresponding to about 6 cm of delay within the satellite line of sight are observed towards the northwest edge of the interferogram (*Figures 10 and 11a*), just east of the City of Buffalo with a correlation between the InSAR phase delays and a spike in SWE equivalence for the date Dec. 04, 2010 (*Figure 11*). Sharp correlations between the InSAR phase and SWE for the date Jan. 19, 2011 are not as apparent; however the total phase change is a combination of snow from both dates. By differencing the SWE data along profile (*Figure 11d*) in we see the resultant profile resembles that of the InSAR data illustrating the combined effects from both dates.

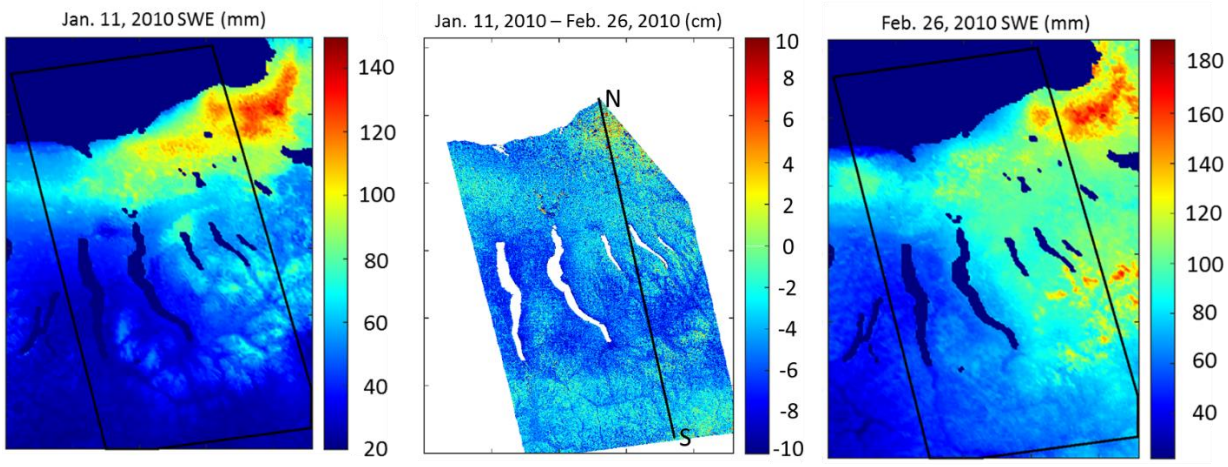

Figure 12: Interferometric phase changes associated with snow for the dates Jan. 11, 2010 – Feb. 26, 2010 from Track 135 (center), and SNODAS SWE models corresponding to each date (left and right).

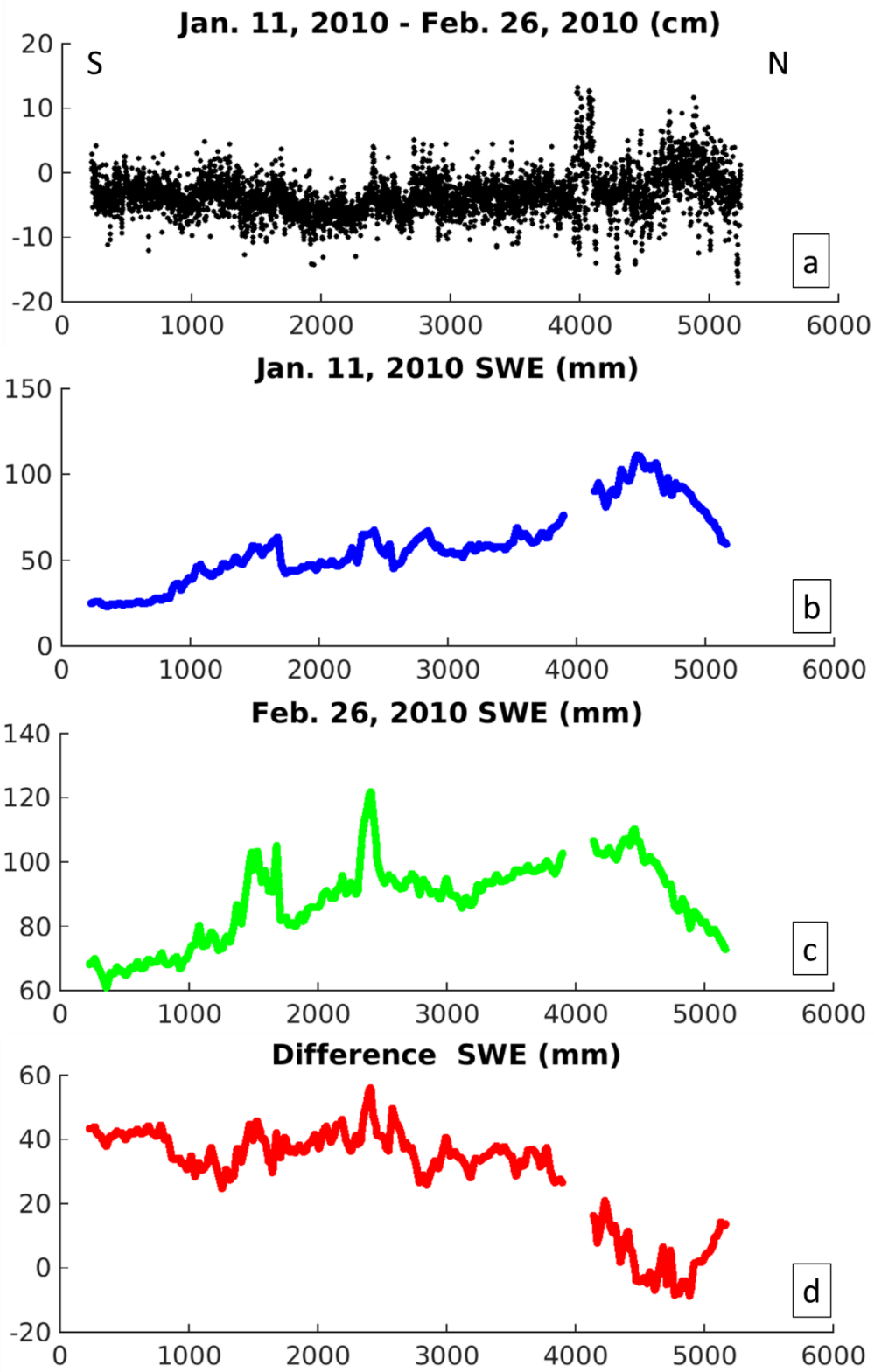

Figure 13: Profiles of the interferogram from Jan. 11, 2010 – Feb. 26, 2010 (a) and of the corresponding SWE models (b and c) for each date, and the difference of the SWE models (Feb. 26, 2010 minus Jan. 11, 2010) (d). Location of the profiles is shown in Figure 12.

The interferogram spanning Jan. 11, 2010 – Feb. 26, 2010 from Track 135 is another good example of the combined effects of snow from two winter scenes (*Figure 12*). Similar quantities of SWE are found in the northeastern section of the interferogram, with slightly higher SWE content in the first date Jan. 11, 2010, similar to previous example, however, the resulting LOS phase change is positive on order of 2 – 3 cm towards the satellite. This illustrates the point that SWE data is good for cross-correlations with the InSAR data to identify phase delays from snow, but significantly more information or analyses of the physical properties of the snow pack is needed to derive relationships between InSAR phase delays and SWE or vice versa. As a side note, by observing spatial distribution of InSAR phase and SWE in Figure 12, we find that topographic features in the InSAR data corresponds well to similarly topographically correlated locations in the SWE data. The similarity of InSAR, SWE, and topography data can be further explored, but is best pursued with quantitative cross-correlation methods instead of qualitative assessments presented in this thesis. Examples of interferograms constructed with a single winter date containing snow are shown in Figures 14, 15, 16. Clear spatial correlations between InSAR phase and SWE can be observed, however, the SWE cannot explain all features in the InSAR phase as factors such as atmospheric effects must also be considered for a comprehensive study of the topic.

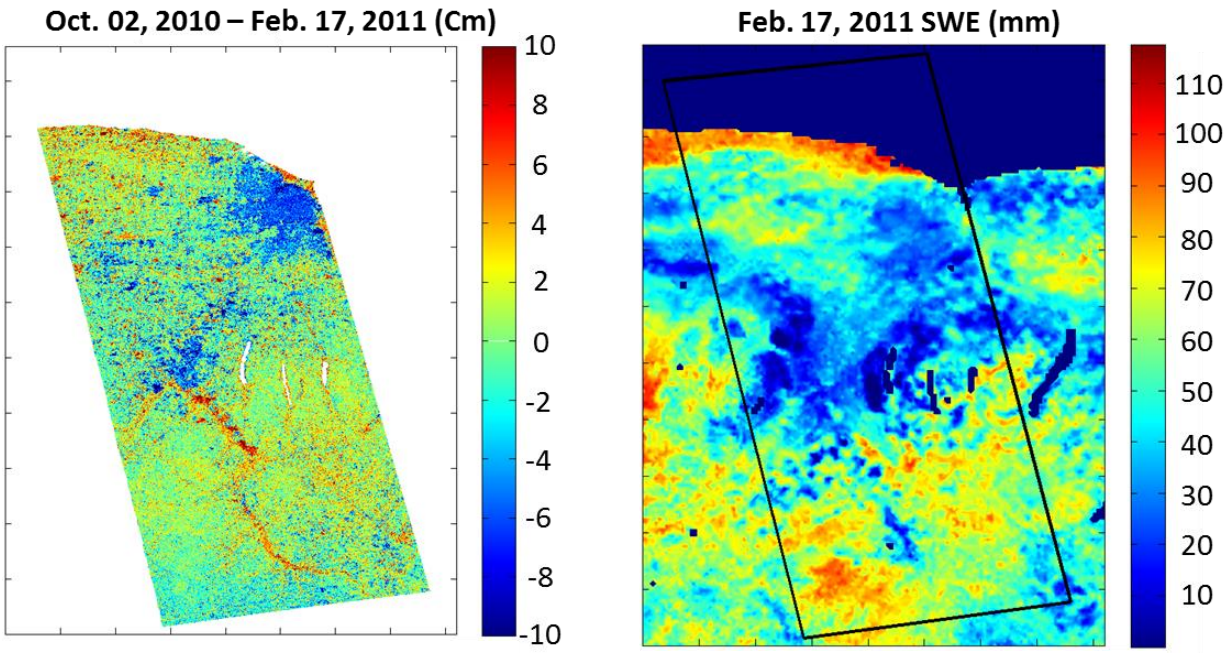

Figure 14: Interferometric phase changes associated with snow for the date pair Oct. 02, 2010 – Feb. 17, 2011 from Track 137 (left), and the SNODAS SWE model corresponding to Feb. 17, 2011 (right).

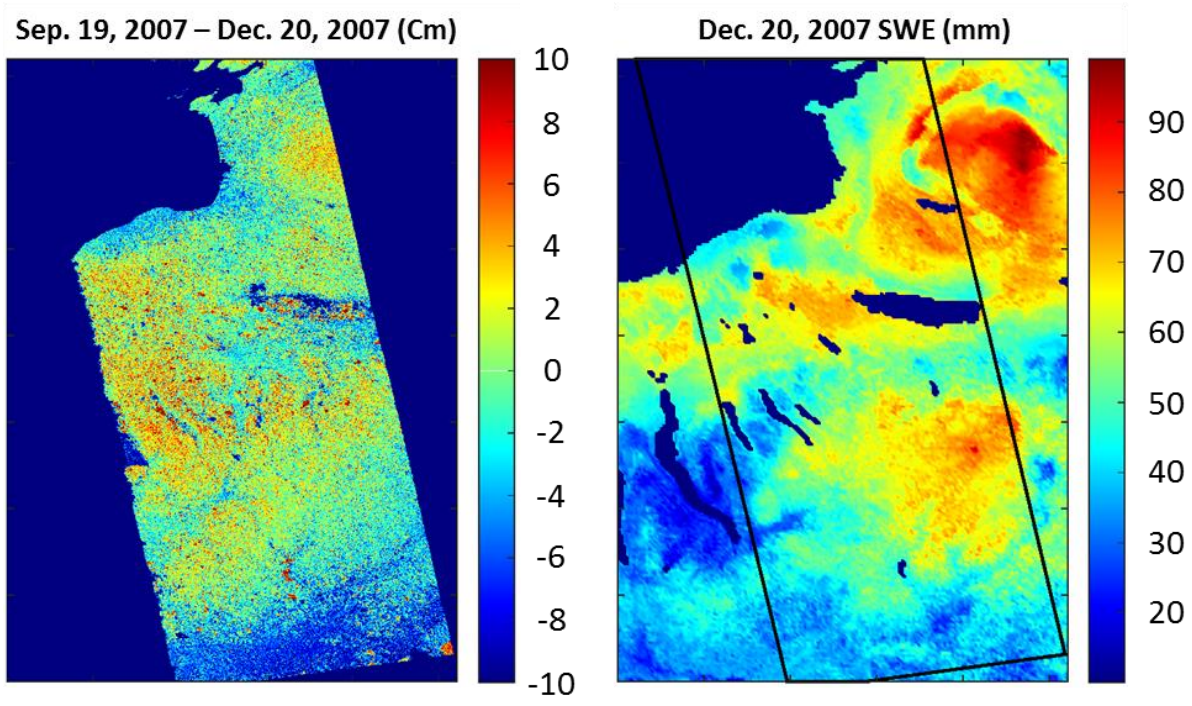

Figure 15: Interferometric phase changes associated with snow for the date pair Sep. 19, 2007 – Dec. 20, 2007 from Track 134 (left), and the SNODAS SWE model corresponding to Dec. 20, 2007 (right).

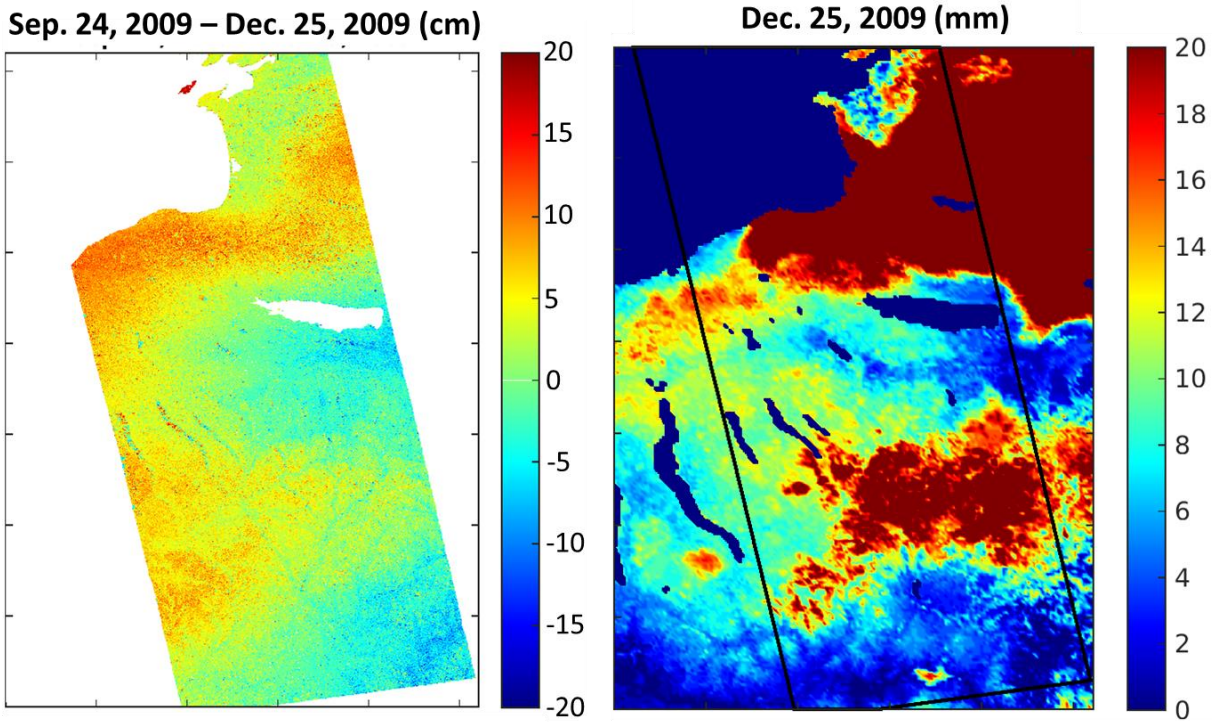

Figure 16: Interferometric phase changes associated with snow for the date pair Sep. 24, 2009 – Dec. 25, 2009 from Track 137 (left), and the SNODAS SWE model corresponding to Dec. 25, 2009 (right).

5.3 American Rock Salt Mine

The American Rock Salt (ARS) Mine in Livingston County, NY was founded in 1997 and is the largest producing rock salt mine in the US. It has been in operation since the early 2000's and has a current production capacity of about 4.5 million short tons per year (Bolen, 2015). The mine is located to the east of the Genesee Valley at a depth of about 540 ± 100 meters beneath the surface extending over a roughly 4.5 km by 2.5 km area. The ARS Mine planned on using extraction ratios of 40 – 60% around pillars and an extraction ratio of 21% near existing shafts according to a prospective proposal for the mine (Akzo Hampton Corners subsidence report, 1995). At the ARS Mine, leakage of groundwater is less of a concern that it

was at the nearby Retsof Mine since the mine does not underlie large glacial valley aquifers, such as those that were associated with the disastrous flooding at the nearby Retsof location.

Subsidence rates above the ARS Mine were anticipated not to exceed rates experienced at the nearby Retsof mine site due to the utilization of larger support pillars than were used at Retsof. Estimated total subsidence over the room panels with an extraction ratio of 60% at the ARS Mine was predicted by Akzo to be 3.0, 6.5, and 26.0 inches after 5, 10, and 50 years following the start of extraction respectively (Akzo Hampton Corners subsidence report, 1995), corresponding to rates of 1.5, 1.6 and, 1.3 cm/yr. As shown below, out results and those of the mine's own repeat leveling surveys indicate much higher rates.

5.4 Geology

The Silurian and Devonian strata in the vicinity of the ARS Mine consists of an approximately 540 meter thick section with a layer of overlying glacial till. At the base of the Devonian sequence, the Onondaga Formation is an approximately 42 meter thick limestone layer that rests unconformably on the Bertie Limestone. The contact of the two limestone bearing formations hosts small bedrock aquifers within the neighboring Genesee Valley. Shales overlay the Onondaga formation and contain two smaller limestone layers, the Tichenor and Centerfield units (Yager et al., 2001; Smith et al, 2005).

The Vernon formation is divided into A, B, and C units. The B unit contains a number of significant salt layers that can be traced throughout most of the Appalachian Basin (Rickard, 1970). The salt layer currently mined by the ARS Mine is the Vernon B6 subunit. The B6 subunit ranges in thickness from 4 – 9 meters and the top of the unit ranges in depth from about 440 – 640 meters from the surface in the vicinity of the ARS Mine (Smith et al., 2005 and Yager

et al., 2001). The depth to the top of the B6 subunit increases as the unit extends to the South dipping at a few degrees (Lugart et al., 2006).

5.5 InSAR time series for the American Rock Salt Mine

ALOS-1 data covering the ARS Mine consists of two overlapping tracks with 14 and 12 scenes respectively that collectively span the time period from 22 December, 2006 to 24 March, 2011. Following phase unwrapping and removal of poor interferograms (based on decorrelation or independent data confirming the presence of snow), we have 17 and 10 interferograms for tracks 137 and 138, respectively (*Table 2, Figure 17*). The ALOS-1 orbit drifted significantly over time, by design, for the benefit of studies on vegetation structure that required spatial separation (perpendicular baseline) between images. This drift is clearly visible in Figure 17. Because correlation decreases rapidly with increasing spatial baseline, this necessitates the construction of long temporal baselines to maintain temporal continuity for the time series.

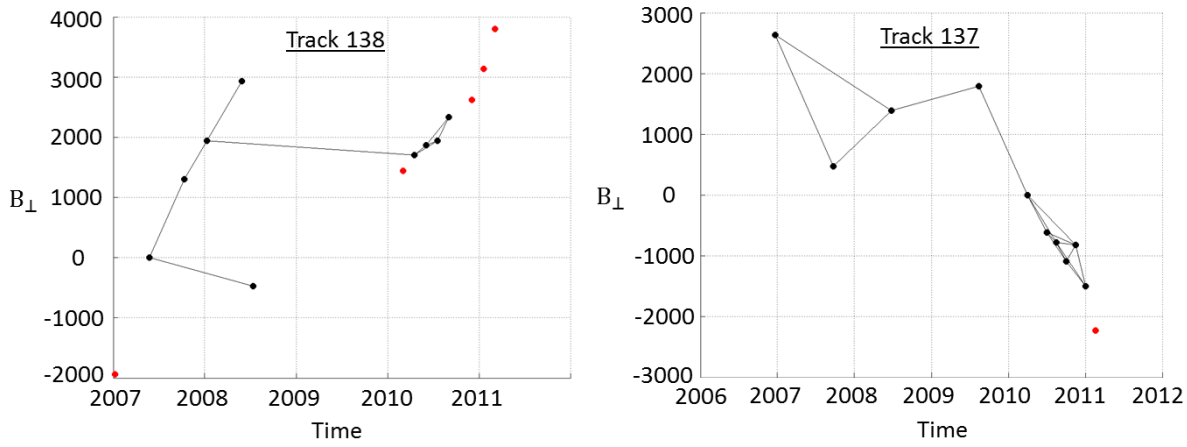

Figure 17: Perpendicular baseline vs. time for interferograms used in InSAR time series analysis for Tracks 138 and 137. Dots indicate the date and spatial baseline of each image relative to a master image (baseline = 0). Red dots indicate dates that exhibited significant effects from snow cover and that were taken out of the analysis.

Average rate maps for Tracks 137 and 138 (*Figures 18 and 19*) illustrate the general quality of the data. The density of PS pixels is generally greatest within urbanized areas, such as the city of Rochester, and lowest around rivers and in the Genesee Valley. Overall, the scatter of the time series in regions that are not expected to experience deformation is approximately ±1.6 cm/yr.

Table 2: Interferograms used to make time series.

Interferogram	$B_{\perp}$ (m)	Time (days)	Track
Jun. 26, 2008 - Aug. 14, 2009	395	414	Track 137
Sep. 24, 2007 - Jun. 26, 2008	921	276	Track 137
Apr. 01, 2010 - Aug. 17, 2010	-780	138	Track 137
Jul. 02, 2010 - Aug. 17, 2010	-167	46	Track 137
Apr. 01, 2010 - Nov. 17, 2010	-822	230	Track 137
Aug. 17, 2010 - Nov. 17, 2010	-42	92	Track 137
Jul. 02, 2010 - Nov. 17, 2010	-210	138	Track 137
Oct. 02, 2010 - Nov. 17, 2010	265	46	Track 137
Apr. 01, 2010 - Jul. 02, 2010	-612	92	Track 137
Aug. 17, 2010 - Oct. 02, 2010	-307	46	Track 137
Jul. 02, 2010 - Oct. 02, 2010	-475	92	Track 137
Aug. 17, 2010 - Jan. 02, 2011	-715	138	Track 137
Nov. 17, 2010 - Jan. 02, 2011	-673	46	Track 137
Oct. 02, 2010 - Jan. 02, 2011	-408	92	Track 137
Dec. 22, 2006 - Sep. 24, 2007	-2162	276	Track 137
Dec. 22, 2006 - Jun. 26, 2008	-1241	552	Track 137
Aug. 14, 2009 - Apr. 01, 2010	-1788	230	Track 137
May 26, 2007 - Oct. 11, 2007	1305	138	Track 138
Oct. 11, 2007 - Jan. 11, 2008	639	92	Track 138
Jan. 11, 2008 - May 28, 2008	985	138	Track 138
Apr. 18, 2010 - Jun. 03, 2010	163	46	Track 138
Apr. 19, 2010 - Jul. 19, 2010	237	92	Track 138
Jun. 03, 2010 - Jul. 19, 2010	74	46	Track 138
Jun. 03, 2010 - Sep. 03, 2010	462	92	Track 138
Jul. 19, 2010 - Sep. 03, 2010	388	46	Track 138
May 26, 2007 - Jul. 13, 2008	-473	414	Track 138
Jan. 11, 2008 - Apr. 18, 2010	-237	828	Track 138

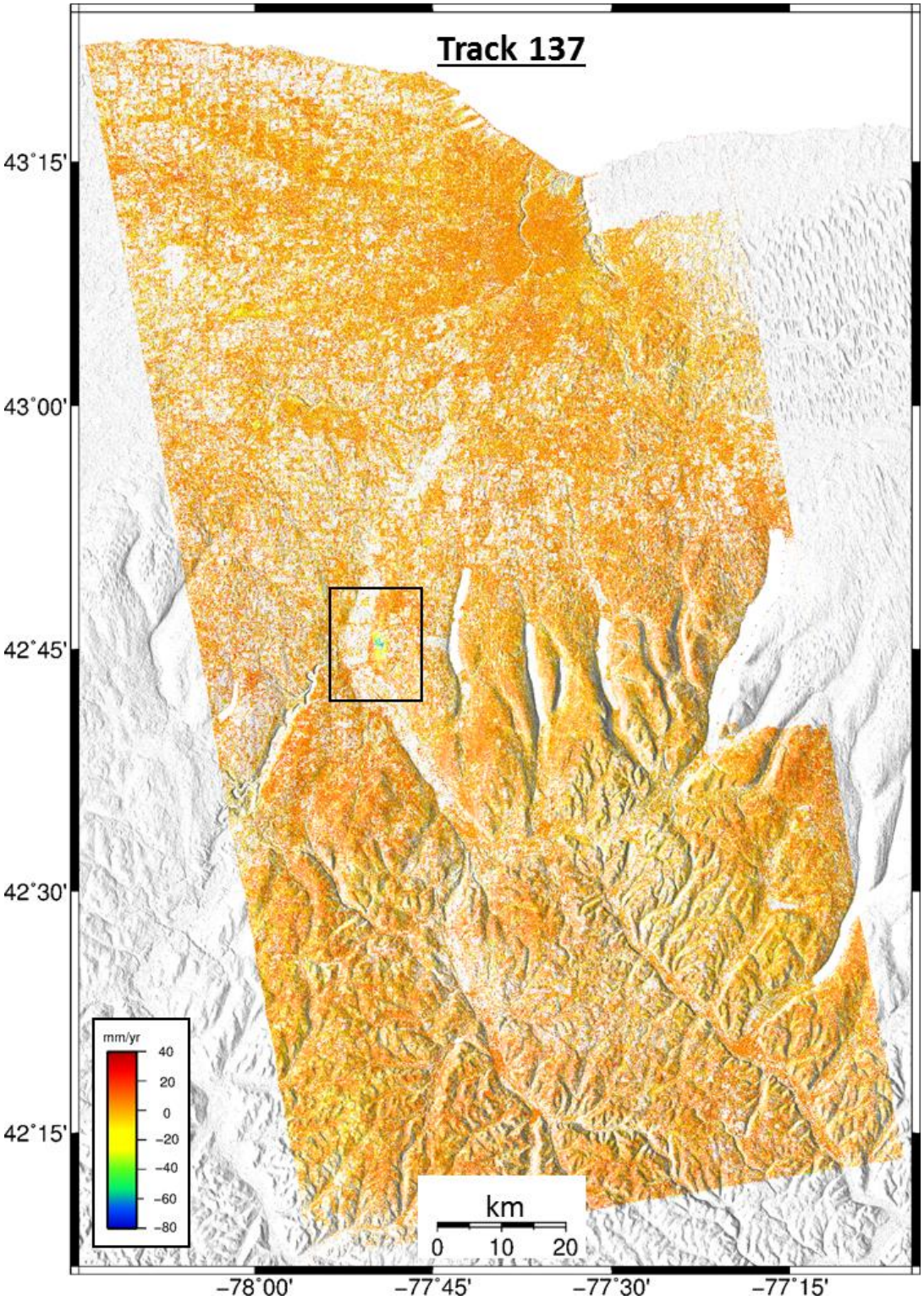

Figure 18: Average line-of-sight rates for Track 137, overlain on shaded topographic relief. Gray areas indicate regions that were not covered by Track 137, or that were masked out due to poor pixel quality. Box indicates area shown in later figures.

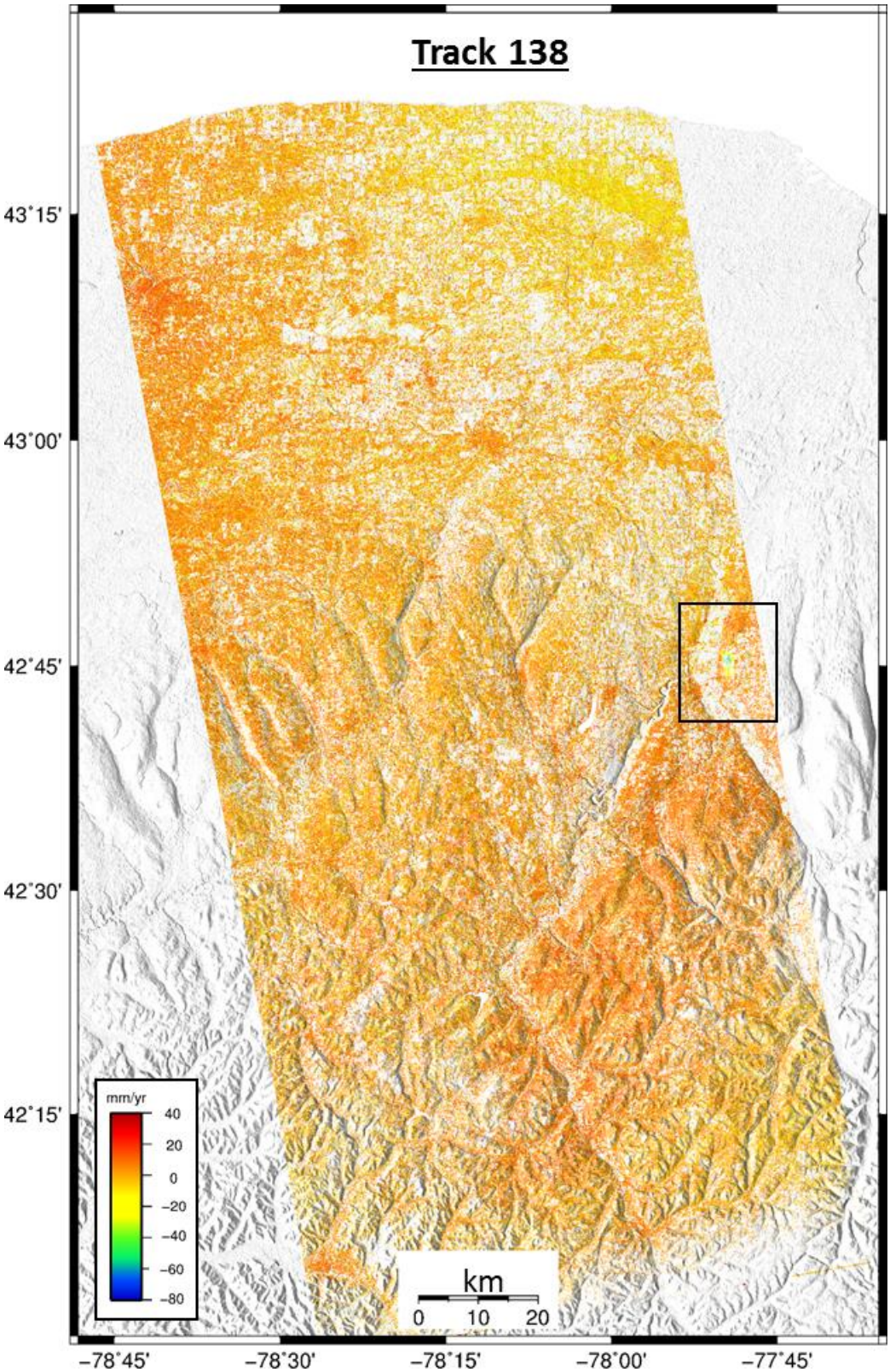

Figure 19: Average rates for Track 138. Annotations as in Figure 18.

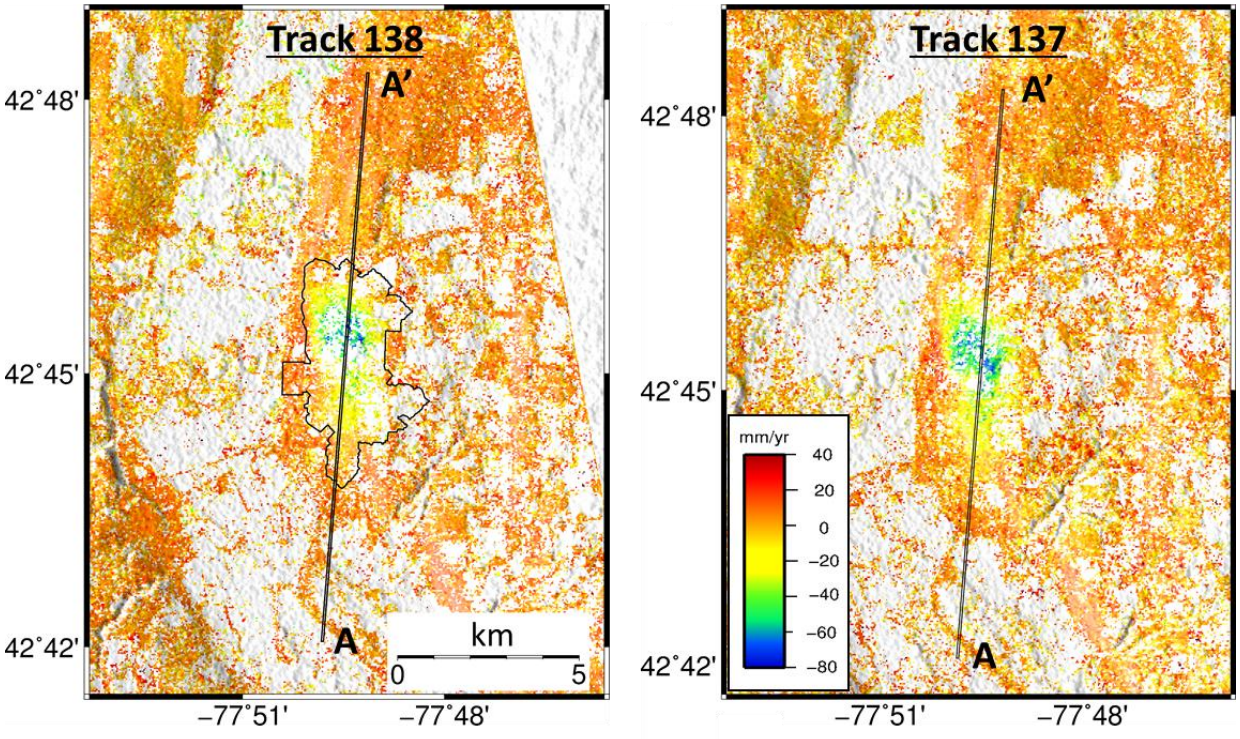

Figure 20: Average rate maps over the location of the ARS Mine for Tracks 138 and 137. The outline of the ARS Mine for the year 2011 is overlain rates for Track 138, and the black line from A to A' shows the location of the profile in Figure 21. The scale bar and color scale are the same for both images.

East of the Genesee Valley, an approximately 5 km by 2.5 km subsidence signal exists in the time series from each track, corresponding well to the location of the ARS Mine. Subsidence of the ARS Mine is confined to within the bounds of the mine extent (*Figure 20*) with good spatial agreement between average rates for both satellite tracks and generally good agreement for the magnitude of subsidence (*Figure 21*). Maximum subsidence rates within the satellite LOS are approximately 80 mm/yr towards the upper center of the mine which decrease towards the edges of the mining area. The shape of the subsidence basin is skewed to the north with subsidence dropping off rapidly at the northern end of the mine and gradual decaying towards the south end (*Figure 21*). Figure 21 shows sharp perturbations in the LOS rate at locations

approximately 2000 meters and 3000 meters north and south of the subsidence area respectively. These perturbations could reflect effects from vegetation or soil moisture.

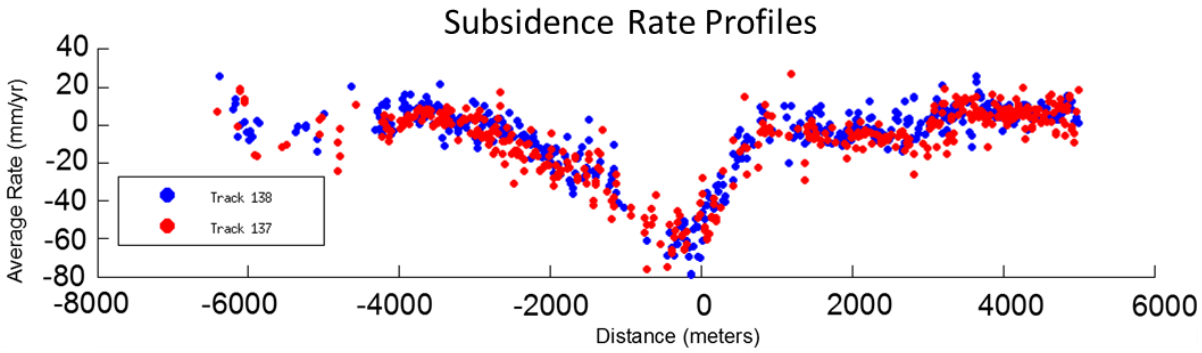

Figure 21: Profile of the average rates across the subsidence basin for both Tracks 138 (blue) and 137 (red).

Generally for regions in the mine that were excavated prior to the earliest image acquisition in the time series, the observed subsidence in the InSAR time series is linear (*Figures 22 & 23*) with uncertainty of ~0.9 cm/yr. Some pixels show signs of slowing subsidence rates towards the end of the time series, but leveling data obtained after 2011 shows a continuation of linear subsidence and so we attribute any signs of slowing to scatter in the data. Error bounds for each data point in the time series were estimated by calculating the variance in a 200x200 pixel region north of the mine for each cumulative deformation map. Scatter in the data varies spatially; however, variance estimates over the total of all non-deforming areas yields similar results. As expected, urban regions such as the city of Rochester have smaller variances. Uncertainty on the rates was estimated by generating 1000 variants of each time series per pixel using the estimated variances for each data point and assuming a Gaussian distribution of the data errors. The variance of the 1000 different rates for each pixel yielded an estimate of the uncertainty. This is a simplified analysis of the data uncertainty, as a full treatment of the

uncertainty necessitates the analysis of many factors including noise sources (e.g., atmospheric phase delays) in individual interferograms, spatial correlations of the data, and data coherency among others, and is beyond the scope of this thesis.

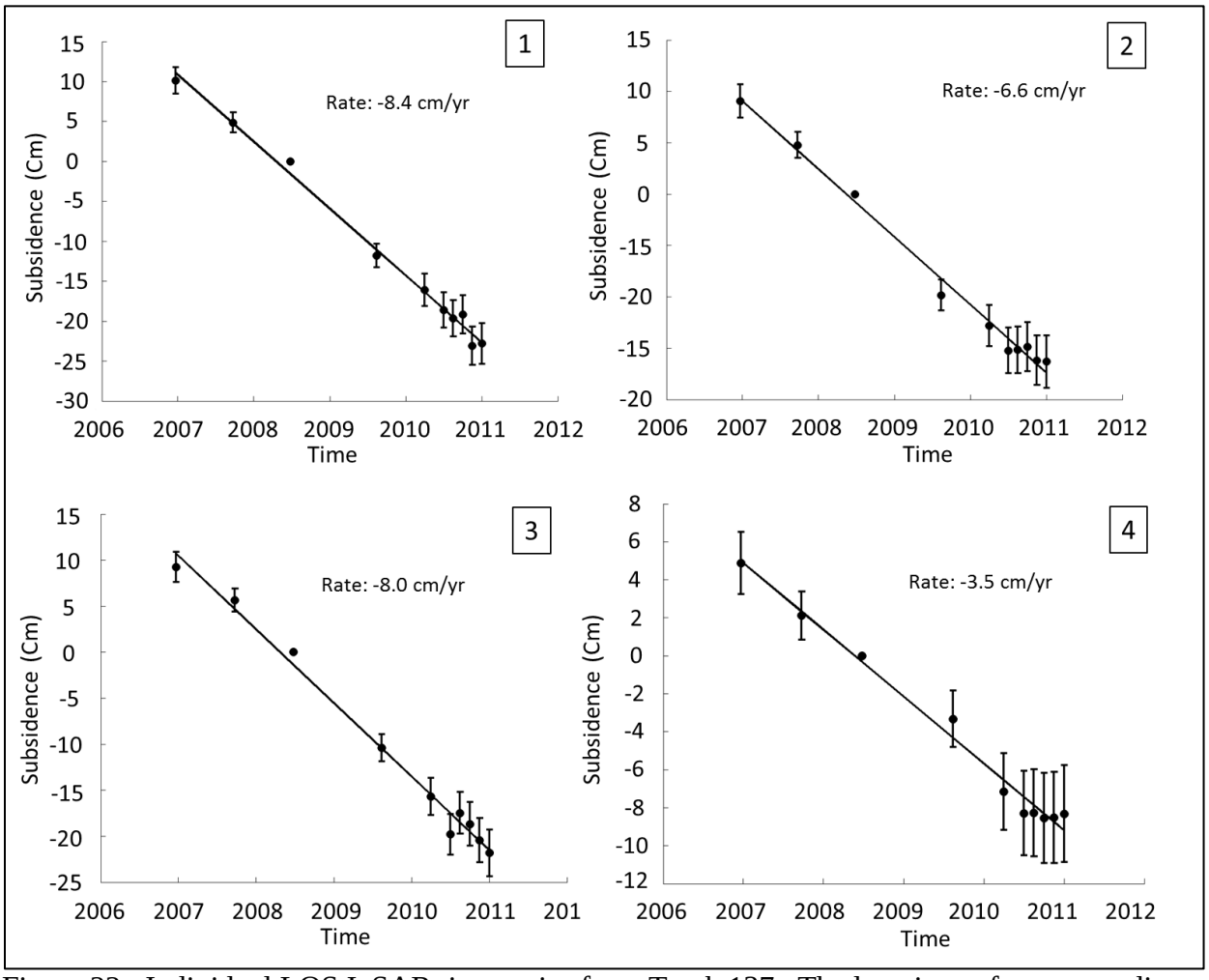

Figure 22: Individual LOS InSAR time series from Track 137. The locations of corresponding pixels are shown in Figure 24.

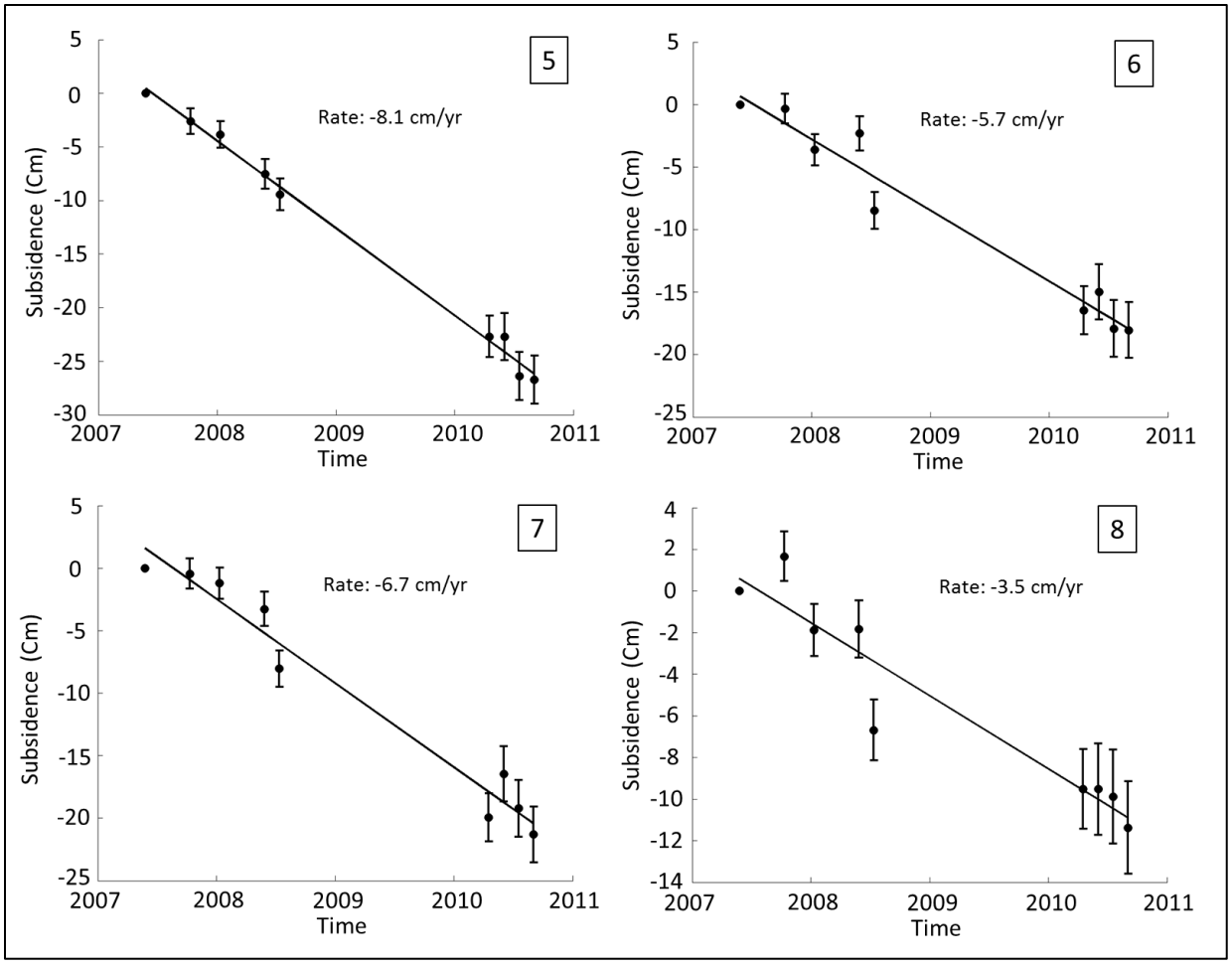

Figure 23: Individual LOS InSAR time series from Track 138. The locations of corresponding pixels are shown in Figure 24.

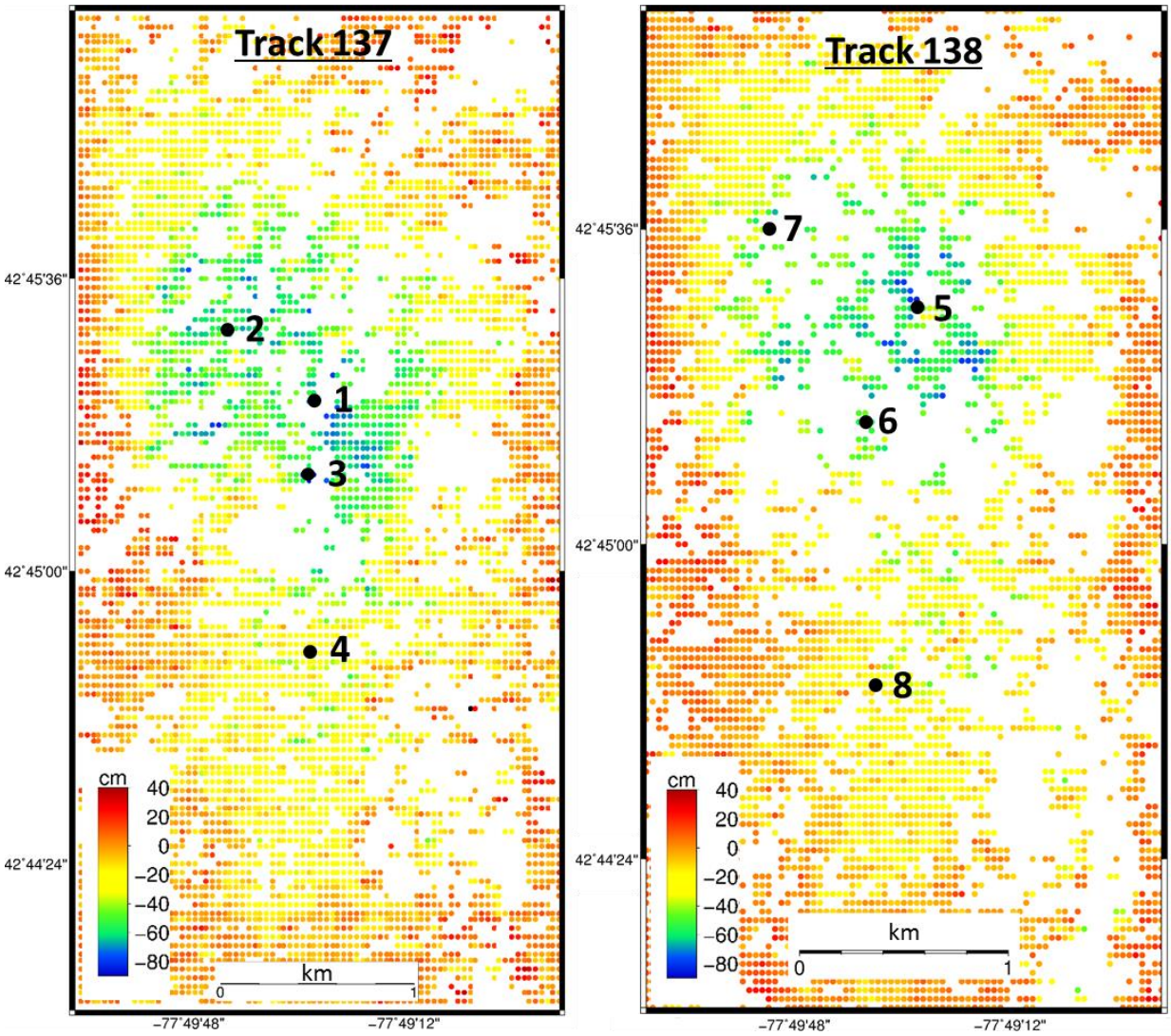

Figure 24: Average rates for Tracks 137 and 138 with pixel locations of the time series plots in Figure 22 and 23.

The reported expansion of the mine between Dec. 2006 to Dec. 2011 is shown in Figure 25. Some areas of the mine that were excavated near the beginning or during the time of image acquisitions display non-linear subsidence time series likely corresponding to the primary creep stage of the rock salt pillars (*Figure 25*) as the front of the mine activity passed beneath them. Time variable subsidence rates are not observed in all sections of the mine excavated within the time frame of the image acquisitions, but are primarily found towards the upper center to most northern ends of the mine. To assist in identifying locations of time variable subsidence, we used a "delayed linear" fit for each time series pixel. The fit was performed by incrementally fixing the intercept of a line at different values and inverting for the slope while all points preceding the time-intercept of the resultant linear fit were set to zero. Multiple residual maps for each fit including the linear fit, were generated, and for each pixel, the fit that produced the minimum residual was recorded as an index number. Plotting the spatial distribution of the numbers reveals locations which are more likely subsiding non-linearly (*Figure 25*). A significant number of pixels in the northern section of the mine, are found to have non-linear deformation characteristics (*Figure 25*). Examples of non-linearly deforming pixels are shown in Figure 26. Generally, significant deviations from zero and transition to linear rates occurs around mid to late 2008 for the northern area which is consistent with the timing of the mine front; however, an area in the northern section of the mine for Track 138 makes this transition around 2010. An example of such a time series is shown in Figure 26, plot 4. The mine face advanced beyond this locations and the large time gap between late 2008 and early 2010 in the time series makes timing of the transition poorly resolved.

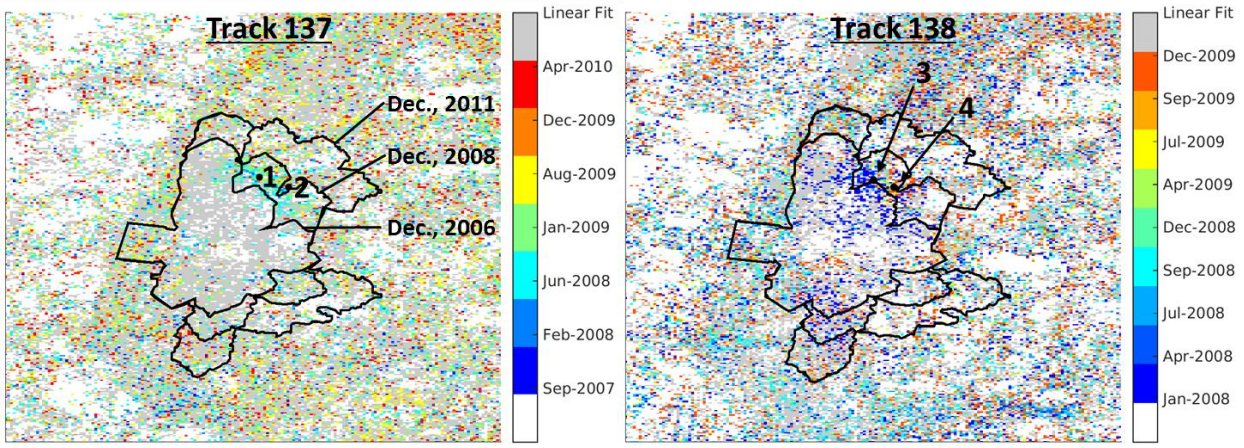

Figure 25: The locations of pixels likely exhibiting non-linear subsidence are shown in red to blue colors, and the locations of linearly deforming pixels are shown in gray. The outline of the ARS Mine is plotted overtop showing the spatial extent and advancement over the years 2006, 2008, and 2011.

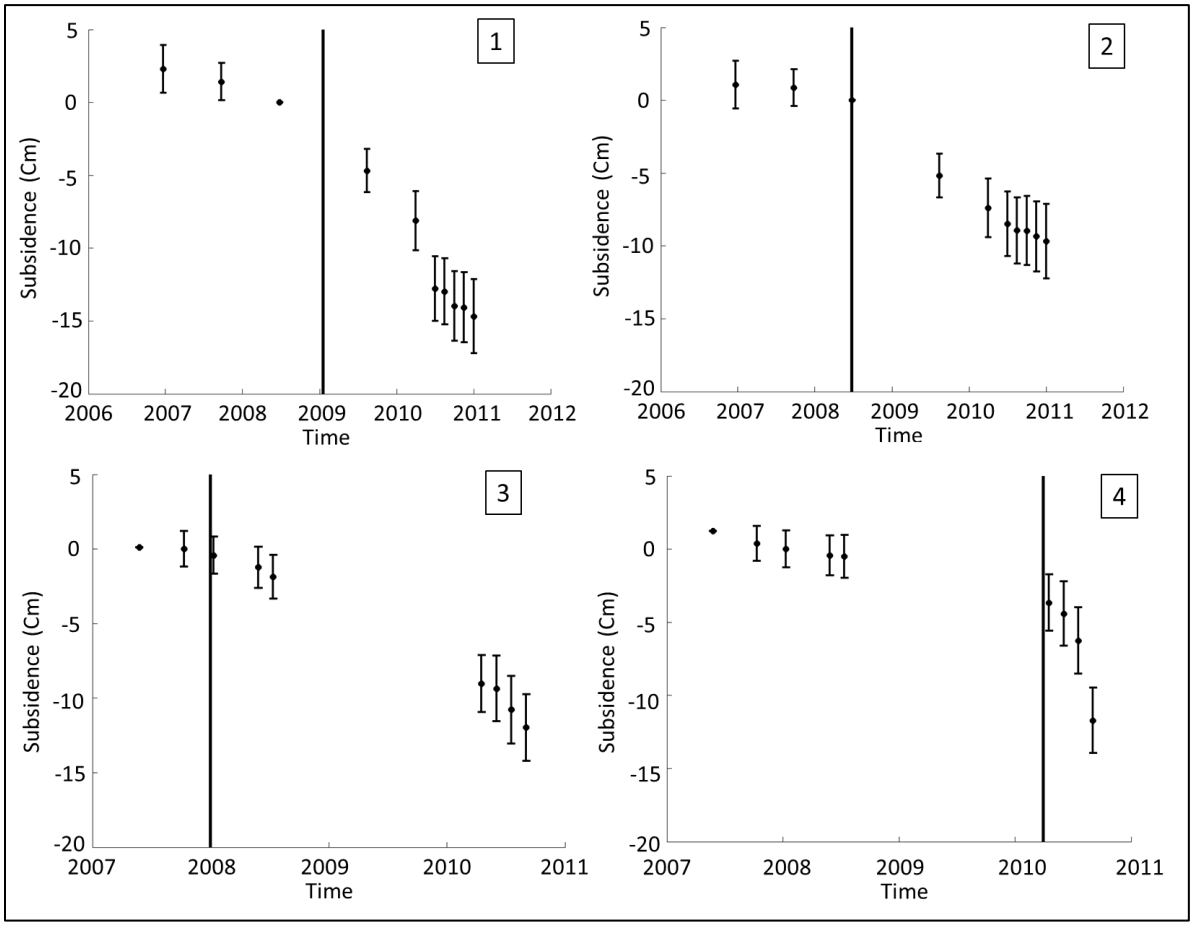

Figure 26: Time series plots for pixels exhibiting time variable subsidence rates. The locations of each pixel are indicated in Figure 25. Vertical black lines indicate times when each time series deviates from zero.

5.6 Comparison of InSAR and leveling data

Leveling, a common method used for monitoring mine subsidence, can yield elevation measurements at point locations with millimeter scale accuracy. For the purposes of this thesis, we use the leveling data provided by the American Rock Salt Company to test the accuracy of InSAR measurements at leveling points.

A large array of 408 monuments are positioned in multiple lines above the ARS Mine from which annual leveling surveys were completed from the years 2000 to 2015. For ease of comparison, we only used leveling data obtained from Oct. 2006 – Oct. 2011, the same time period as spanned by the InSAR data. Leveling monuments are often damaged or lost and reliable measurements cannot be taken, so points which had one or no measurements acquired over the time period were removed from the analysis. The resulting dataset consists of 370 monument locations (*Figure 27*).

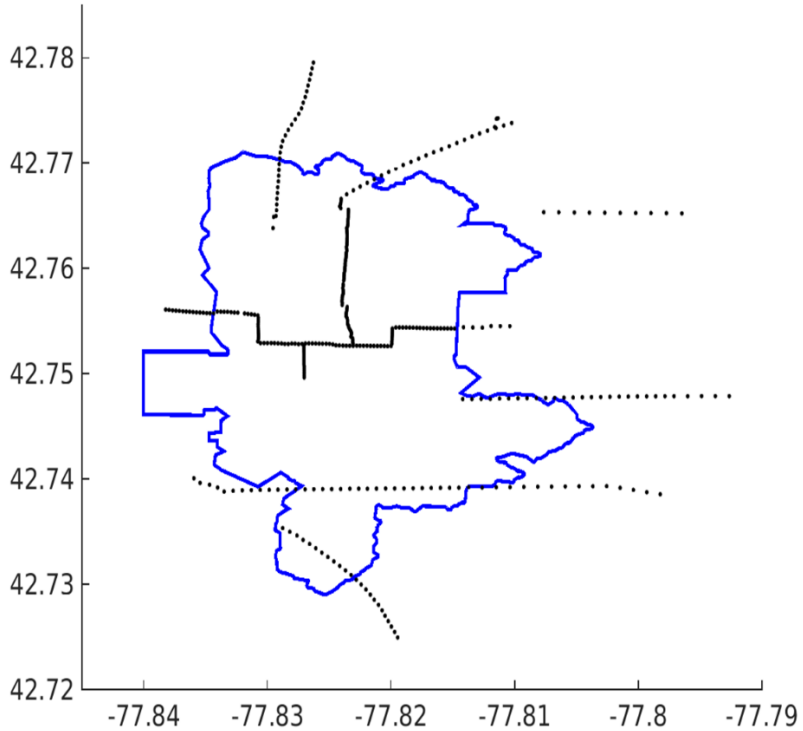

Figure 27: Monument locations from the ARS Company leveling surveys used in this analysis. Locations are plotted over the mine outline for the year 2011.

Average rates estimated from the leveling time series (*Figure 28*) shows that the leveling data varies smoothly across mine region and defines an area of subsidence generally agreeing with the InSAR data. Maximum subsidence rates from leveling are about 0.7 cm/yr greater than the maximum LOS rates obtained from the InSAR time series, and about 4.2 cm/yr greater than InSAR derived LOS subsidence rates corresponding to monument locations (*Figure 29*). Since the InSAR observations are within the satellite LOS, part of the rate discrepancy can be partly accounted for by applying an incidence angle correction to the InSAR data. Better agreement between the two datasets is attained (e.g., *Figure 29*); however, the InSAR measurements of subsidence are still significantly lower than the leveling.

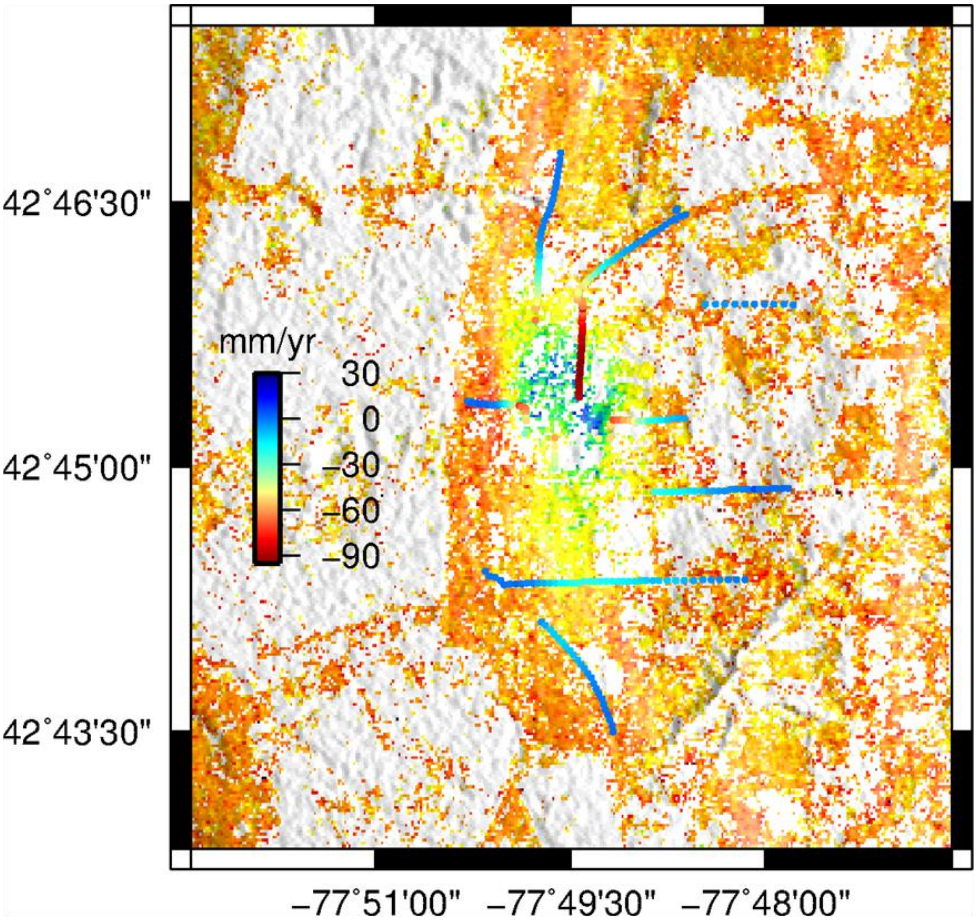

Figure 28: Locations of the leveling monuments plotted over the LOS average rate map for track 137 (Color scale same as Figure 20). The red – blue color scale indicates the average rate of vertical ground deformation at each monument location.

To estimate the difference between InSAR and leveling rates, we calculated the means of nine InSAR pixels surrounding each monument location and differenced the results with the corresponding leveling rates. The results are summarized in Figure 30, and mean differences between rates are 1.50 and 1.63 cm/yr for Tracks 137 and 138 respectively. Scatterplots (*Figure 30*) show relatively good correspondence of rates within range of 0 – 2 cm/yr and a zone with significantly poorer agreement (~6.5 – 9 cm/yr). Observation of the spatial distribution of residuals (*Figure 31*) from the rate comparison reveals that high discrepancies for both tracks are concentrated in a region towards the north end of the subsidence basin. We find that the InSAR and leveling datasets differ most in the region corresponding well to the locations of non-linear subsidence. Besides errors from data acquisition or processing, disparities between InSAR and leveling rates can be attributed to a few potential causes: differences in temporal spacing of data points, seasonal biases in InSAR data, and horizontal surface displacements towards the satellite.

In the areas of non-linear subsidence, the estimated average rate will be reduced if a larger time interval is considered. The leveling data is available for the time period from Oct. 2006 to Oct. 2011 while the InSAR data covers the time range Dec. 22, 2006 to Jan. 02, 2011 and May 26, 2007 to Sep. 03, 2010 for Tracks 137 and 138 respectively. The leveling observations are spaced evenly every October within the time period. Differences in the temporal span of each of the datasets is relatively small and the temporal span of the InSAR data is within the span of the leveling data, however, a number of leveling points towards the northern most extent of the survey do not have data for Oct. 2006. For these points, the leveling data spans from Oct. 2007 to Oct. 2011. The difference in temporal span may potentially have an effect on the estimated rates, however, a majority of points with large rate difference cannot be explained by this reasoning.

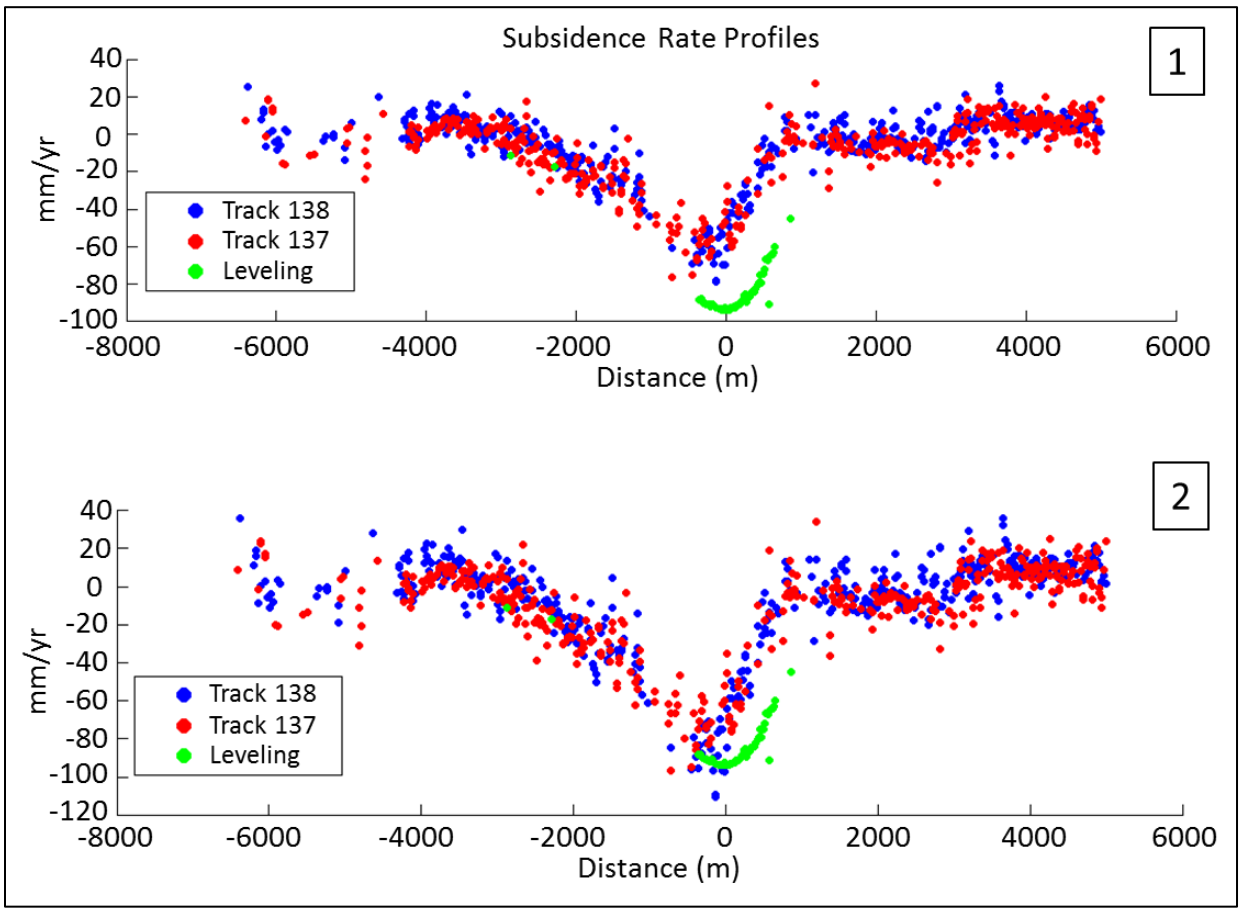

Figure 29: Profiles comparing InSAR rates with rates from leveling for InSAR line-of-sight measurements (1) and InSAR corrected for the incidence angle (2) under the assumption that deformation is vertical.

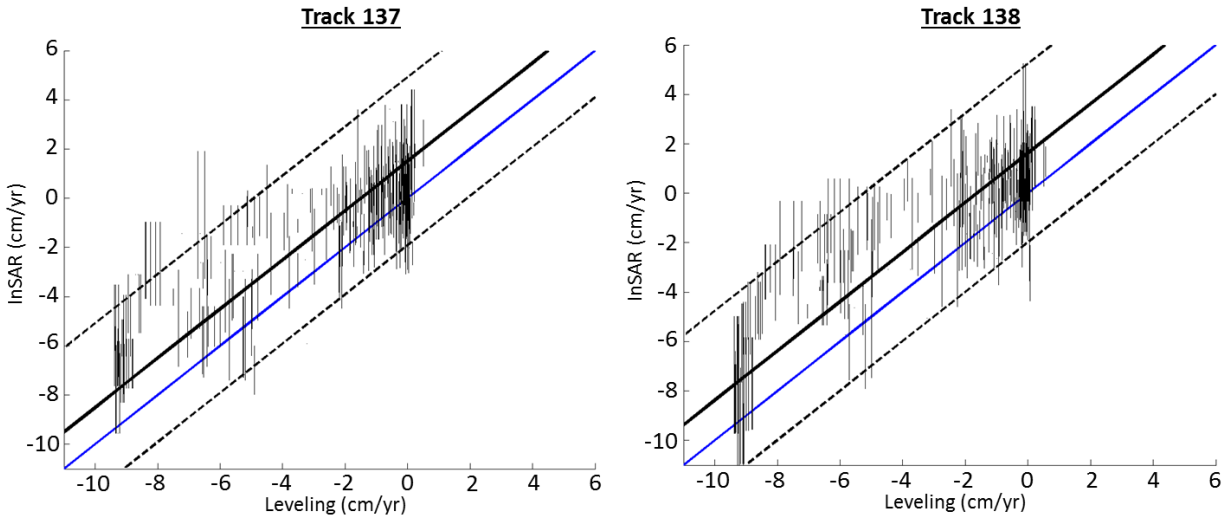

Figure 30: Comparison of leveling rates with the average rate of nine InSAR pixels surrounding each leveling point plotted as lines showing the maximum and minimum for each cluster of InSAR pixels. Data lines that fall on the blue line indicate good agreement between rates, the black line shows the average difference offset of the rates, and the dashed lines show RMS error. Mean differences in rates are 1.50 and 1.63 cm/yr for Tracks 137 and 138 respectively.

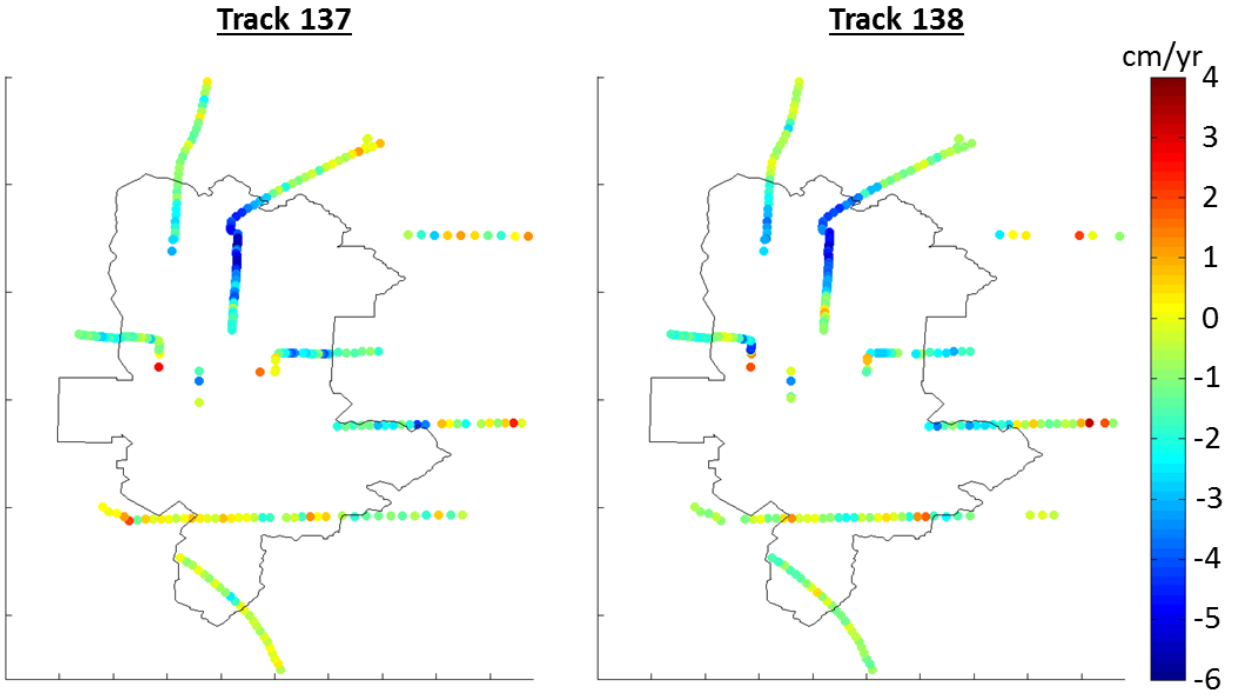

Figure 31: Residual between leveling and InSAR rates in cm/yr.

Two examples of individual time series corresponding to the region of highest rate differences at the north end of the mine shows that InSAR generally does a poor job of resolving subsidence from about 2007 to 2009 (Figure 32). For the Track 137 time series, there appears to be better agreement between the slopes of leveling and InSAR trends from 2009 to 2010. Following 2009, the Track 138 time series does not show easily distinguished trends due to a limited number of dates clustered between 2010 and 2011. To explore the possibility of better agreement in the linear portion of the time series for each dataset, average rates are inverted for using only dates following the start of 2009 for both leveling and the Track 137 dataset. The comparison of obtained rates and residuals are given in Figure 33. Overall, there is better agreement between the two datasets with a mean difference of 1.45 cm/yr compared to the previous 1.50 cm/yr for Track 137. Discrepancies around -8 cm/yr in Figure 30 are improved as shown in Figure 33.

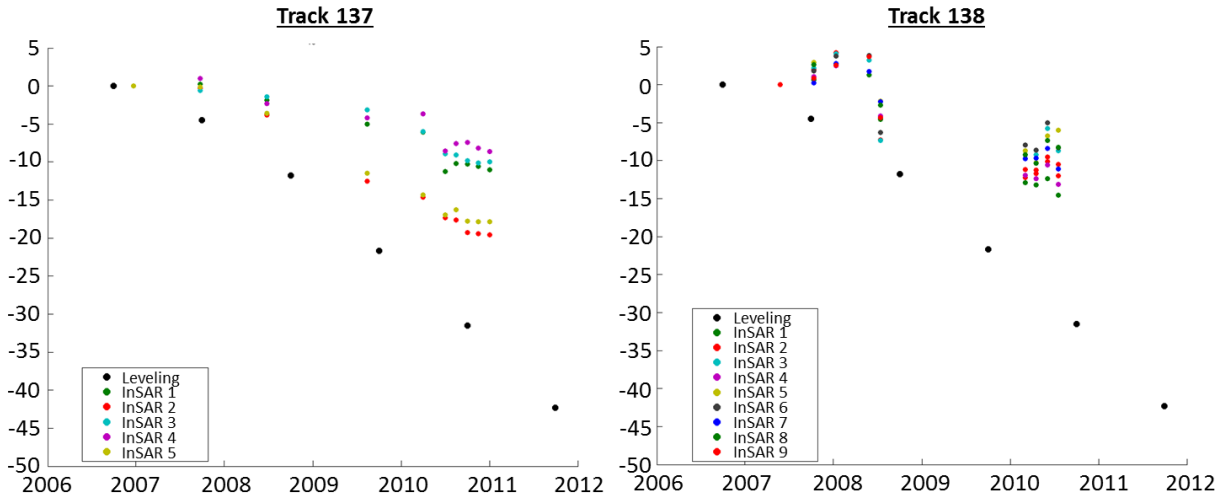

Figure 32: Representative examples of leveling and InSAR time series in the region of highest rate discrepancy towards the northern end of the mine shown in Figure 31. Leveling time series is given by the solid black dots while colored dots indicate different time series for pixels in a 3 by 3 box around the leveling location.

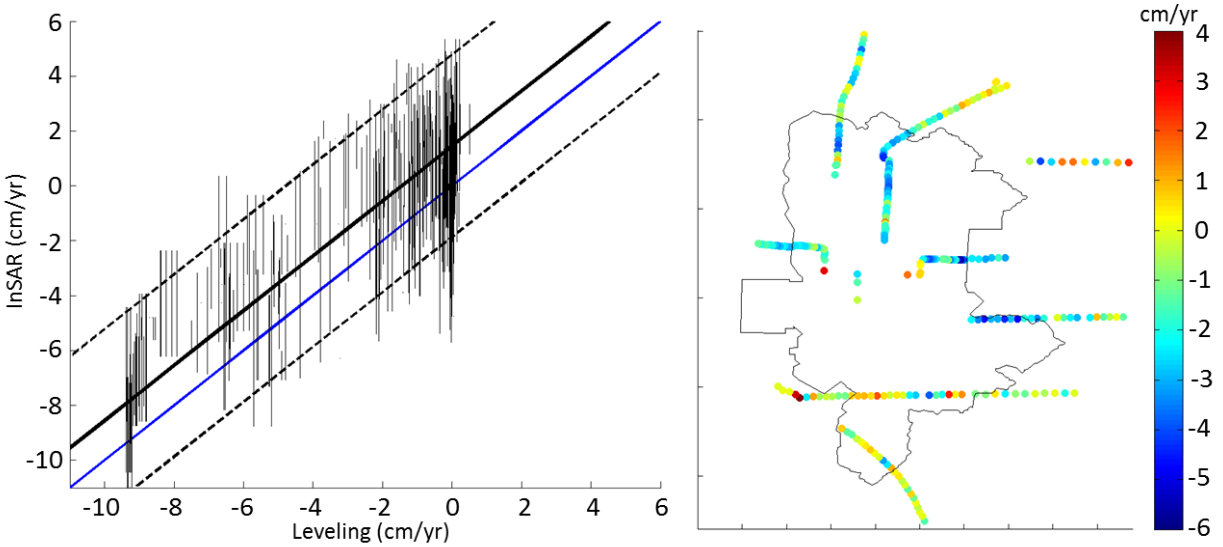

Figure 33: Comparison of InSAR and leveling rates obtained from inversion of only dates from 2009 to 2011. Left: scatter plot of average rates for InSAR (y-axis) and leveling (x-axis) where the range of InSAR rates for a 3 by 3 box of pixels around each leveling location are indicated by the vertical black lines. The black solid line indicates the mean difference between rates. Right: residual map of leveling and InSAR rates.

The residuals in the northern section of the mine a decreased to ~2 – 3 cm/yr compared to the previous ~4 – 6 cm/yr, however, other areas show increased residuals such as towards the eastern side of the mine typified by linear subsidence. Using only a portion of the available time series in linearly deforming areas could naturally lead to slightly worse agreement between InSAR and leveling. Generally, there is an improved fit between the datasets in the northern section of the mine where greatest residual was previously observed.

Seasonal variations in surface properties (e.g., soil moisture) or seasonal variations in surface height from ground water fluctuations could potentially bias the estimated InSAR subsidence. The leveling data was acquired every year in October indicating that the leveling time series would be less sensitive to seasonal variations in ground movement, whereas the time series for the InSAR data is comprised of interferograms containing combinations of spring, summer, and fall dates. Assuming that ground motions associated with ground water occur on a

seasonal basis with fluctuations in surface height on order of ±10 mm, it is possible that the dates could be distributed along the seasonal cycle such that a bias is introduced. Similarly, effects from soil moisture in interferograms could potentially bias the InSAR time series. Variations in soil moisture content between time periods can have effects on the interferometric phase. Increases in soil moisture content causes both the ground to sell and the ground penetration depth of the SAR radiation to decrease (e.g., Nolan et al., 2003). Both effects result in a line of sight shortening of the interferometric phase which acts as an increase in the estimated surface height. For subsidence signals, this could potentially reduce the amount of observed downward displacements ultimately biasing the time series. Conversely, both of these processes could act to bias the InSAR time series such that greater subsidence is observed. The bias of the time series depends on the temporal sampling of the SAR dates relative to seasonal processes.

It is possible that at the northern end of the subsidence basin horizontal surface displacements (which were neglected in our assumption that the displacements were vertical) primarily result in motion towards the satellite. Such displacements could detract from the magnitude of observed surface subsidence within the satellite line of sight. This possibility is explored in later sections through modeling to obtain north-south, west-east, and vertical components of surface displacements and project them into the satellite LOS.

5.7 Modeling

To model convergence of the mine roof, we inverted InSAR derived average subsidence rates for vertical displacements across a sub horizontal plane within an elastic medium using the equations for tensile slip on a plane (Okada, 1985). By inverting for mine convergence, we can

obtain estimates of the 3D displacement field at the surface by forward modeling of the inversion results.

Inversions of full InSAR datasets involves potentially millions of points which is computationally expensive, hence InSAR data is often spatially averaged for model inversions (e.g., Lohman and Simons, 2005). We spatially average rate maps for each satellite track using an algorithm developed by Lohman and Simons (2005) which is based on the data resolution matrix with a certain level of smoothing to reduce the number of data points, while maintaining the general information content of the data (Lohman and Simons, 2005). Results of the spatially averaged rate maps used for the inversions are shown in Figure 37.

The plane used in the inversion has dimensions of 5 × 2 km (north and east axes), and is centered at 540 meters depth with a dip of 4 degrees to the south. The plane is partitioned into 30 × 15 patches along the north-south and east-west directions respectively, yielding individual patch sizes of about 167 by 133 meters with 450 total patches. A Green's function was found, relating unit slip to resultant displacements at the locations of InSAR data points on the surface, by running a forward with the Okada model for each patch. The resulting displacements for each patch yielded an $N \times N_{patch}$ Green's matrix, G_i, where N is the number of data points and N_{patch} is the number of patches (i.e., 450). A Green's matrix was formed for the resampled average rate maps of each InSAR track and combined to form a single design matrix (e.g., equation 5.1). The design matrix and resampled data vector were weighted by the inverse of the Cholesky factorization of the data variance matrix given by C_{d_i}, where the data variance is given by the slope variance of the InSAR average rates. For the inversion, we have

$$\begin{bmatrix} G_1 C_{d_1} \\ G_2 C_{d_2} \end{bmatrix} [m_{model}] = \begin{bmatrix} d_1 C_{d_1} \\ d_2 C_{d_2} \end{bmatrix}, \tag{5.1}$$

where d_i are the resampled InSAR data and m_{model} is the vector of model parameters.

The inversion was smoothed with a Laplacian operator yielding an $N_{patch} \times N_{patch}$ smoothing matrix, κ, with the amount of smoothing determined by the parameter λ_s. Additionally, a zero slip condition was enforced on patches outside of the mine region excluding patches partially contained within the mine region. This was achieved with an $N_{patch} \times N_{patch}$ damping matrix, η, whose values consists of ones corresponding to the locations of target fault patches and zeros elsewhere. An arbitrarily large damping factor, β, was applied to minimize the slip on these outside-mine patches. The resulting inversion is given by

$$\begin{bmatrix} G_1 C_{d_1} \\ G_2 C_{d_2} \\ \kappa\lambda_s \\ \eta\beta \end{bmatrix} [m_{model}] = \begin{bmatrix} d_1 C_{d_1} \\ d_2 C_{d_2} \\ 0 \\ 0 \end{bmatrix}. \quad (5.2)$$

Depending on the value of the smoothing parameter, λ_s, there is a tradeoff in the fit to the observed data and roughness of the model solution. By varying the value of λ_s we can plot the model roughness vs. the solution residual to yield the resulting L-curve (*Figure 34*). The smoothing value is chosen to minimize the solution error while producing a reasonably smooth model (e.g., *Figure 36*).

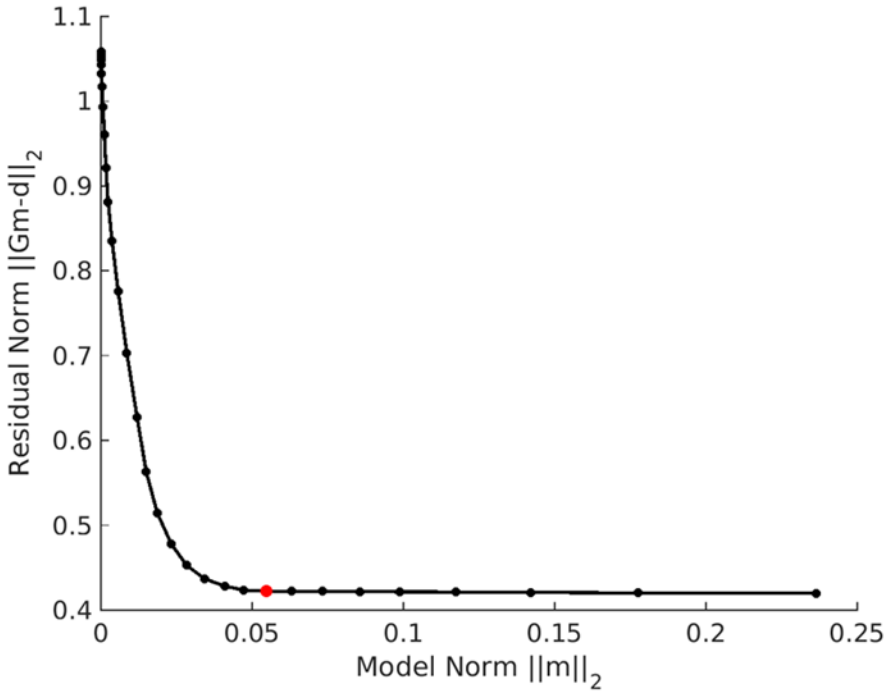

Figure 34: L-curve for the model norm vs. residual norm for different smoothing values. The amount of smoothing is chosen to minimize solution residual while yielding a reasonably smooth model solution where the red dot indicates the chosen value for λ_s.

Observation of the model resolution matrix (Figure 35) can determine if there are patches poorly resolved in the inversion. Diagonal values of one indicate patches that are perfectly resolved whereas patches that are not perfectly resolved show a distribution of values collectively summing to one centered on the diagonal such as in Figure 35. The resolution is generally similar for each of the patches with slightly higher resolution on the edges of the plane. Irregular partitioning of the plane can be performed based on resolution of each patch, however we do not explore the refinement of the plane patches, as the current partitioning is found to be satisfactory in the model inversion.

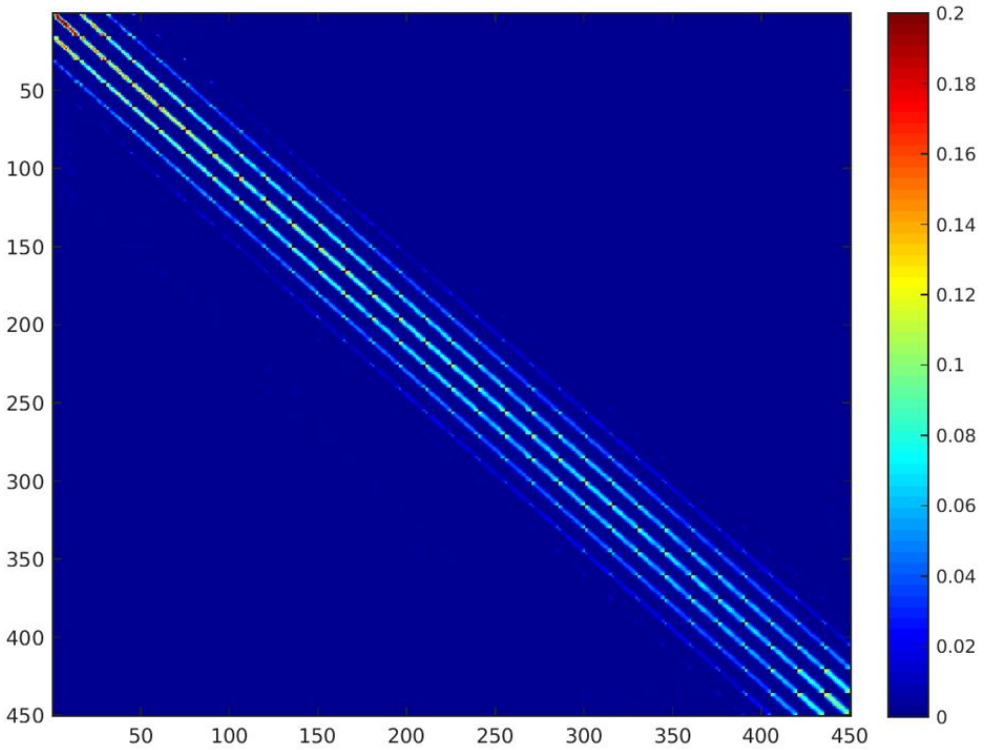

Figure 35: Model resolution matrix for the inversion.

We solve for the model parameters using a non-negative least squares solution such that slip on the plane is solely convergent. The solution varies relatively smoothly with convergence concentrated more on the right hand side of the mine, and maximum convergence rates are approximately 13 cm/yr towards the center of the plane. (*Figure 36*). Convergence is generally constrained to within the bounds of the mine except for slight amounts of convergence is found at the top right hand corner of the plane far away from the mine area; however, this convergence is negligibly small. We find that the model inversion adequately fits the observed data; however, the tendency for the model solution to concentrate on the right hand side of the mine causes a subsidence deficit in the predicted rates on the west side of the mine, as indicated by a zone of high positive residuals from the model inversion (*Figure 37*).

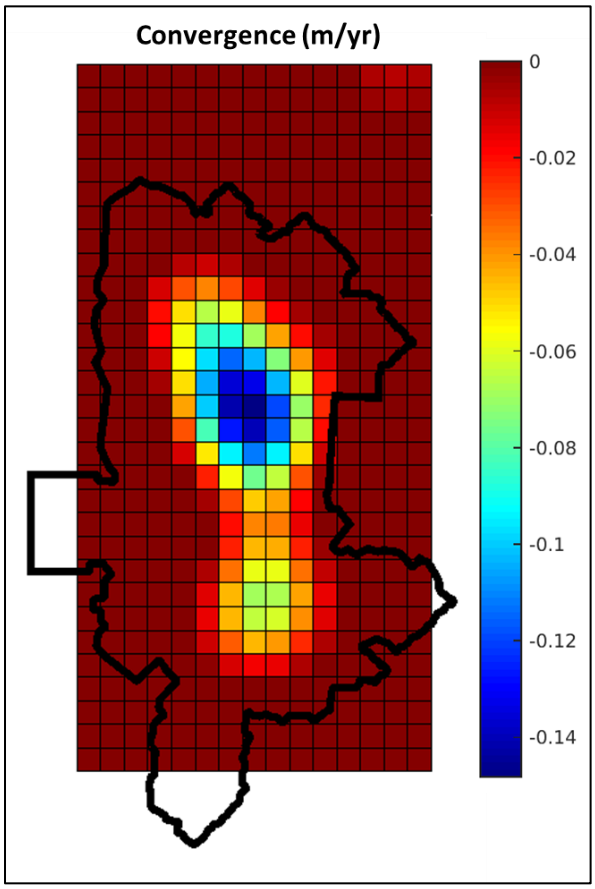

Figure 36: Convergence on a sub-horizontal plane from inversions of InSAR average subsidence rate maps.

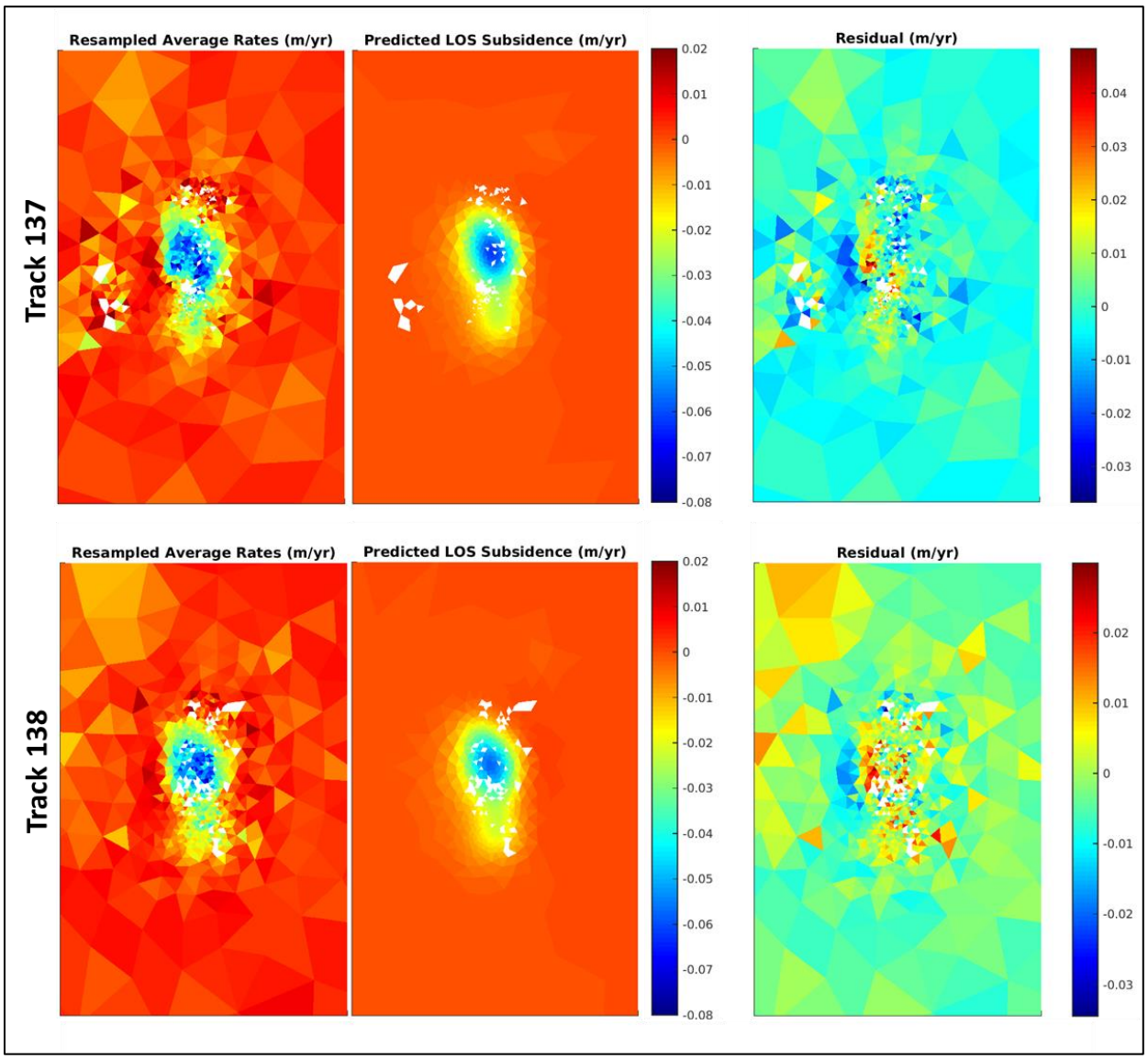

Figure 37: Resampled average rates, predicted average rates from the inversion, and residuals of the observed and predicted subsidence rates for Tracks 137 (top) and 138 (bottom).

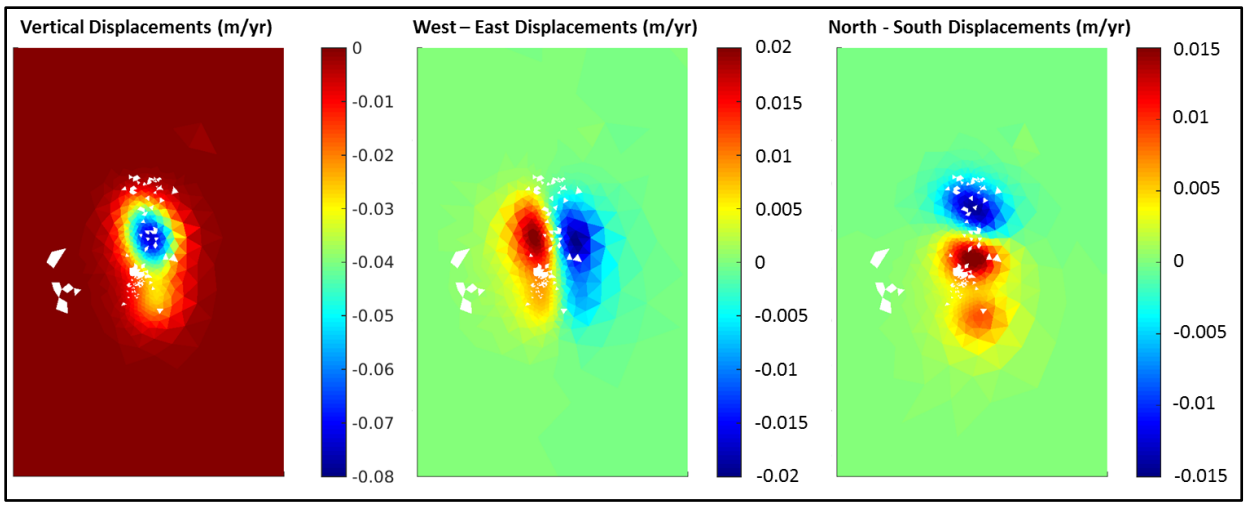

Figure 38: Modeled vertical (left), west-east (center), and north-south (right) components of surface displacements.

To obtain estimates of the 3D surface displacements, we use the Okada (1985) tensile plane solutions to forward model the surface displacements based on the estimates of mine convergence from the inversion (*Figure 38*). We find maximum estimated horizontal displacements of 2 and 1.5 cm/yr for west-east and north-south components respectively. To determine if north-south horizontal surface displacements could detract from the observed LOS subsidence, we project the horizontal displacements into the LOS of the satellite look vector (*Figure 39*). We find that the horizontal displacements at northern end of the subsidence basin project positively into the satellite LOS causing line of sight shortening (i.e., detract from observed subsidence), and coincides well with the location of greatest rate discrepancies between InSAR and leveling. However, only a fraction of the horizontal displacements contribute to the observed LOS displacements, and as seen in Figure 39, only accounts for about 2 mm/yr of displacements which is insufficient to account for discrepancies on order of 2 – 4 cm/yr. The east – west component of displacements acts to increase the observed LOS subsidence on the west side and decrease LOS subsidence on the east side with contributions on order of 1 – 1.5 cm/yr. The east – west component can potentially account for a significant component of the

rate discrepancies observed between the two datasets, however, the leveling locations with greatest difference in rates lies in an area unaffected by the east – west displacements provided by the model. It is possible that the horizontal displacements produced by the model inadequately estimate the horizontal displacement field. The adequacy of the model and potential horizontal contribution to the LOS displacements is best verified by actual measurements of horizontal surface displacements, however, that information is not available during the given time period.

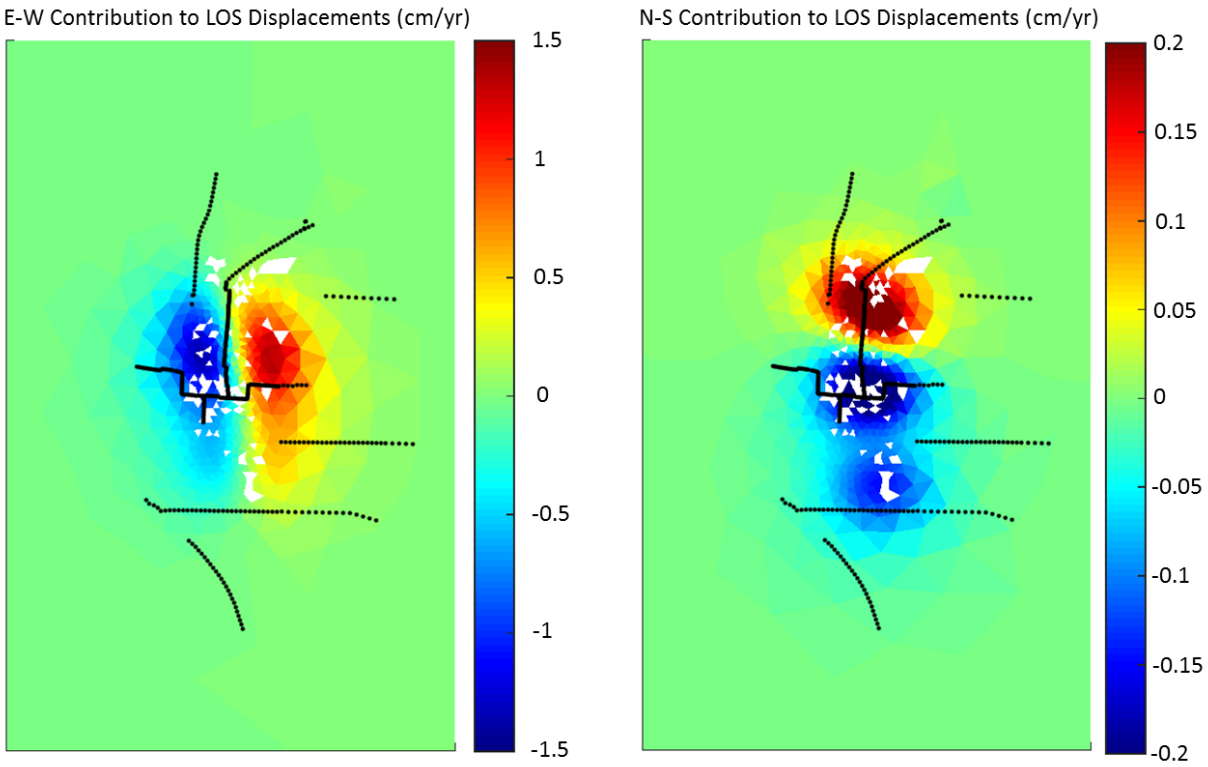

Figure 39: North – south and east – west surface displacements estimated from the model inversion projected into the satellite line of sight. Black points indicate monument locations of the ARS leveling survey.

5.8 Cayuga Salt Mine

The Cayuga Salt Mine resides mostly beneath Cayuga Lake north of the town of Ithaca in Tompkins County (*Figure 8*) with approximately 650 meters of sedimentary overburden. The mine is a room and pillar mine, and uses the yield pillar method (Sambeek, 2012). Because Cayuga Lake overlies a majority of the mine, any potential subsidence beneath the lake cannot be measured by InSAR or other conventional methods. However, a small portion of the mine lies to the east of Cayuga Lake, and any significant subsidence resulting from this section of the mine can be potentially observed with InSAR.

InSAR data coverage over the location of the Cayuga Salt Mine in Tompkins County consists of 12 date acquisitions for Track 135. A total of 32 interferograms were processed observed for signs of subsidence over the location of the mine region. No deformation was observed in either wrapped or unwrapped interferograms corresponding to the location of the salt mine.

5.9 Solution Mining Sites

A number of solution mining sites around western NY are shown in Figure 4. InSAR data corresponding to these locations consists of Tracks 136, 137, 138, and 139. No surface deformation was observed in the InSAR data corresponding to the locations of solution mining sites. The null observation of subsidence in the InSAR data does not rule out the possibility that subsidence is occurring at some of these sites, but rather indicates that if subsidence is occurring, the magnitude of subsidence is beneath the limit of detection by ALOS-1, L-band SAR data. For example, the old solution mining cavities located north of Watkins Glen on the west coast of Seneca Lake (*Figure 8*) is a proposed sight for natural gas storage. Leveling data acquired over

the solution cavity sites indicates that subsidence occurs on average at ~2-3 mm/yr from 2003 – 2013 (US Salt Precise Level Report Watkins Glen Refinery, 2013). Since the scatter in the InSAR time series for the area is on order of 1.5 cm/yr, the subsidence is well beneath the limit of detection by InSAR.

5.10 Landfill

Even though surface subsidence is not observed at other salt mining locations in western NY, we find a relatively small subsidence signal east of the City of Buffalo corresponding well to the location of an old landfill. Landfills that have been resting for some time are known to have large accumulations of methane gas with intermittent degassing events.

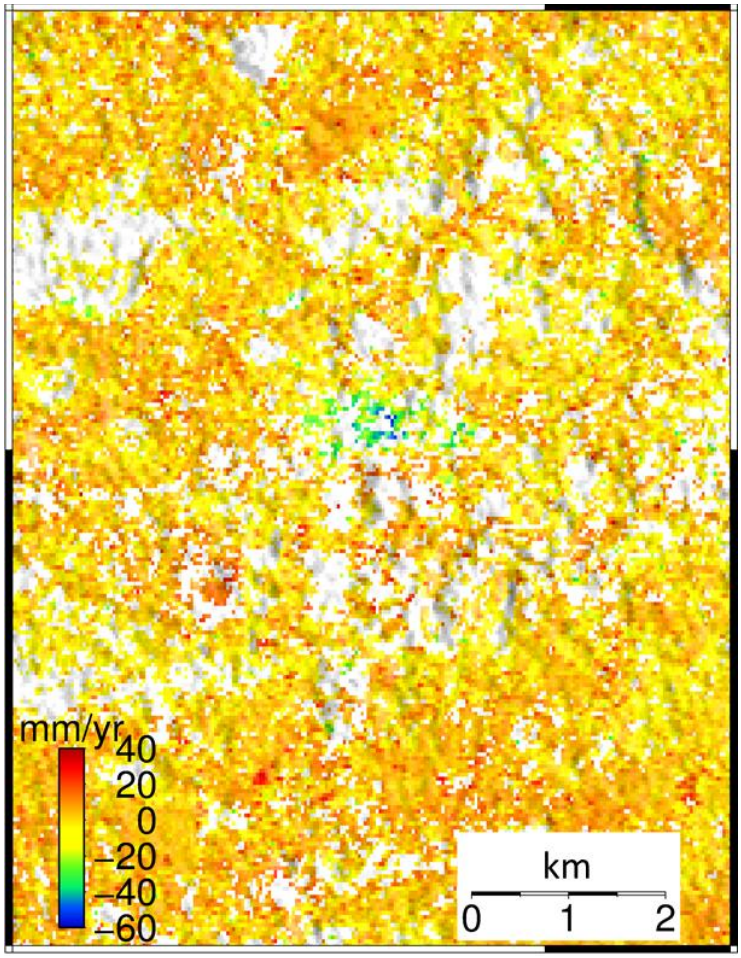

Figure 40: LOS average rates over a landfill east of Buffalo observed in Track 138.

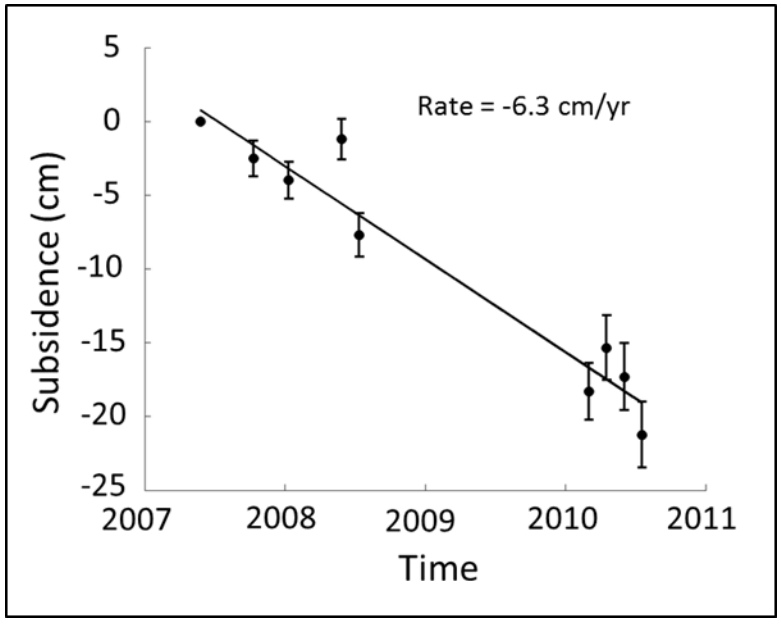

Figure 41: Maximum LOS subsidence time series plot over the landfill shown in Figure 38.

Additionally, as fill materials decay and gas is emitted from the fill, a certain amount of internal compaction can result. As a consequence, we find a 2 × 0.5 km subsidence basin with LOS rates ranging from 3 – 6 cm/yr over the landfill (*Figures 40 and 41*). Such high subsidence rates are well within the limit of detection found for L-band SAR in the region of this study. That being said, the signal resides in an area that contains significant snow cover in a number of images (e.g., *Figure 10*). Comparison of time series that used all dates versus only dates without snow show that, due to higher scatter, subsidence over the landfill would be masked out for the time series using all dates. This signal serves as a good example of potential surface deformation that could be missed as a result of biases from snow.

CHAPTER 6

SUMMARY AND CONCLUSIONS

6.1 Rate Discrepancies and Comparison to Literature

There are a number of studies concerning InSAR measurements of surface subsidence over salt mines (e.g., Wasowski et al., 2007; Nitti et al., 2009; Raucoules et al., 2003; Perski et al., 2009; Kanika et al., 2012). The majority of these studies used ERS 1-2 data (C-band) to monitor surface subsidence and were either in areas with little to no snow cover (e.g., Vauvert France) or where a much larger number of images was available (e.g., Wieliczka, Poland). For studies that compared InSAR derived subsidence estimates with leveling surveys (e.g., Raucoules et al., 2003, Perski et al., 2009), generally better agreement between rates was achieved than was found in this thesis. Raucoules et al. (2003) used 18 interferograms from 16 ERS 1-2 SAR images to make persistent scatterer time series over a solution mine site in Vauvert, France. InSAR subsidence rates were estimated at about 2.2 cm/yr towards the center of the subsidence bowl with the mean difference of 0.16 cm/yr and standard deviation of 0.2 cm/yr between InSAR and leveling data. Perski et al. (2009) used 51 ERS 1-2 images to make persistent scatterer time series over the Wieliczka Mine in Poland. Maximum InSAR subsidence rates measured were about 2.4 cm/yr with rates from leveling on order of 2 mm/yr higher than InSAR rates with some points exceeding discrepancies of 2 cm/yr.

Two other studies (Wasowski et al., 2007; Nitti et al., 2009) focus on subsidence over the Wieliczka Salt Mine. Wasowski et al. (2007) and Nitti et al. (2009) used 39 and 44 ERS 1-2 images respectively to detect subsidence rates of 2.4 cm/yr over the Wieliczka Mine corresponding well with Perski et al. (2009). Good agreement between rates is expected

considering there was much overlap between datasets used. Nitti et al. (2009) also compared L-band (ALOS-1) data with ERS 1-2 data sets over the Wieliczka mine. ALOS-1 data reportedly identified a similar spatial distribution of subsidence, however, with worse accuracy. Exact differences in subsidence rates between datasets were not reported since differences in look angles of the satellites made a direct comparison difficult, however, the worse accuracy of the ALOS-1 data was attributed to the limited number of available images (12 dates).

In this thesis, rates obtained from InSAR agree well between independent sets of SAR data from different, overlapping tracks. However, the rates disagree with leveling rates by a statistically significant amount, although the general spatial pattern agrees. Differences between InSAR and leveling datasets can be potentially attributed to the limited number of available images and temporal sampling of each dataset, similar to the issues found in Nitti et al. (2009). The majority of other InSAR studies, with better agreement, used significantly larger number of images for time series construction than was used in this thesis. Additionally, for this study, seasonal variations of the ground surface could influence subsidence rates from InSAR, whereas leveling data was acquired annually every October reducing potential seasonal biases. Seasonal effects could potentially have greater biases on smaller datasets where the distribution of dates over the year is not uniform. Also, horizontal motion of the land surface within the satellite LOS detracts slightly from the estimated subsidence rates in the area of greatest disagreement between datasets, however, the amount is relatively small compared to the discrepancies between rates.

6.2 General Conclusions

1) The reasonably good results of InSAR data from the L-band ALOS-1 satellite over noisy terrain indicates that more recently deployed satellites will potentially produce better results.

Generally, InSAR has proven useful for monitoring mine subsidence even in areas with dense vegetation and agriculture in addition to intermittent snow cover. The potential effects of snow in other studies should be considered.

2) Longer wavelength L-band SAR allows detection of high subsidence rates over short time periods, in areas with vegetation or snow cover where interferograms using shorter wavelengths would likely decorrelate (e.g., Hongdong et al., 2015). That being said, studies of mine subsidence have found short repeat interval X-band SAR can remain coherent despite adverse ground surfaces (e.g., Kanika et al., 2012) and that more complex processing methods can be implemented to obtain full displacement fields when interferograms decorrelate in areas associated with large surface displacements (e.g., Hongdong et al., 2015).

3) The scatter in this particular InSAR data makes it difficult to observe displacements that are smaller than a few cm/yr. This explains why we do not see deformation at solution mining sites where measured subsidence in expected to be on order of a few mm/yr. This also applies to the Cayuga Salt Mine since the majority of the mine, where maximum subsidence would be expected, resides beneath Cayuga Lake. Only a small on-land portion of the mine, where less subsidence is expected, can be monitored by InSAR. Ongoing significant subsidence is not anticipated at the Retsof mine since the mine is now filled with brine which helps support the overburden. Solution mines, if filled with brine, are also less likely to exhibit the same magnitude of subsidence seen at a room and pillar mine.

4) We find that the sensitivity of ALOS-1 InSAR data set allows detection of non-linear subsidence associated with the progression of subsidence as the mine face advanced despite non-optimal surface conditions and significant scatter in the time series.

5) Generally, the application for InSAR to mine subsidence monitoring appears to be useful even in less than optimal environmental conditions. With newer datasets, the ability of InSAR to monitor mine subsidence is only expected to improve (e.g., TerraSAR-X, NISAR). Newer satellites have improved temporal resolutions (shorter repeat pass intervals) with improved orbital control, both of which serve to decrease image decorrelation and increase sensitivity to surface displacements.

BIBLIOGRAPHY

Akzo Nobel Salt Inc. Hampton Corners Mine Project Appendix D (1995).

Akzo Nobel Salt Inc., et al – Interim Decision January 31, 1996. State of New York Department of Environmental Conservation.

Baar C. (1977), "Applied Salt Rock Mechanics 1: The in-situ behavior of salt rocks", *Elsevier Scientific Publishing Company*, 1.

Berardino, P., G. Fornaro,R. Lanari, and E. Sansosti (2002), A new algorithm for surface deformation monitoring based on small baseline differential SAR interferograms, *IEEE Trans. Geosci. Remote Sens.*,40 (11): 2375–2383.

Bérest P., Brouard B., Feuga B., Karimi-Jafari M. (2008), The 1873 Collapse of the Saint-Maximilien Panel at the Varangeville Salt Mine, *International Journal of Rock Mechanics & Mining Sciences*, 45: 1025 – 1043.

Bolen W. (2015), 2013 Minerals Yearbook: Salt [Advance Release], *US Geological Survey*.

Briggs P. (1996), Salt Mining in New York: The Ins and Outs of the Solution Mining Industry and Its Significance, Meeting Paper.

Brudnik K., Czop M., Motyka J., Obyrn K., Rogoz M., Witczak S. (2010), The Complex Hydrogeology of the Unique Wieliczka Salt Mine, *Przeglad Geologiczny*, 58 (9): 787 – 796.

Burgmann R., Rosen P., Fielding E. (2000), Synthetic Aperture Radar Interferometry to Measure Earth's Surface Topography and Its Deformation, *Annual Rev. Earth Planet Sci.*, 28: 169 – 209.

Carnec C., Delacourt C. (2000), Three Years of Mining Subsidence Monitored by SAR Interferometry, Near Gardanne, France, *Journal of Applied Geophysics*, 43: 43 – 54.

Chen, C.W. and H. Zebker (2002), Phase unwrapping for large SAR interferograms: Statistical segmentation and generalized network models, *IEEE Transactions on Geoscience and Remote Sensing*, 40: 1709-1719.

Chengsheng Y., Qin Z., Chaoying Z., Lingyun J., Wu Z. (2010), Monitoring Mine Collapse by D-InSAR, *Mining Science and Technology*, 20: 696 – 700.

Colesanti, Carlo, et al. (2003), SAR monitoring of progressive and seasonal ground deformation using the permanent scatterers technique, *Geoscience and Remote Sensing, IEEE Transactions on* 41 (7): 1685-1701.

Farr T., Jones C., Liu Z. (2015), Progress Report: Subsidence in the Central Valley, California, Jet Propulsion Laboratory CIT.

Finnegan, N. J., Pritchard, M. E., Lohman, R. B. and Lundgren, P. R. (2008), Constraints on surface deformation in the Seattle, WA, urban corridor from satellite radar interferometry time-series analysis. *Geophysical Journal International*, 174: 29–41.

Goel K., Parizzi A., Adam N. (2011), Salt Mining Induced Subsidence Mapping of Lueneburg (Germany) Using PSI and SBAS Techniques Exploiting ERS and TerraSAR-X Data, *Proc. FRINGE Workshop*, Frascati, Italy.

Guneriussen T., Hogda K., Johnsen H., Lauknes I. (2001), InSAR for Estimation of Changes in Snow Water Equivalent of Dry Snow, *IEEE Transactions on Geoscience and Remote Sensing*, 39 (10): 2101 – 2108.

Hamrin H., (2001), Underground Mining Methods and Applications. *Underground Mining Methods: Engineering Fundamentals and International Case Studies*, Ed. Hustrulid W., Bullock R., Society for Mining, Metallurgy, and Exploration Inc, Hustrid, W.A.

Hongdong F., Gao X., Yang J., Deng K., Yu Y. (2015), Monitoring Mining Subsidence Using a Combination of Phase-Stacking and Offset-Tracking Methods, *Remote Sensing*, 7: 9166 – 9183.

Hooper A., Zebker H., Segall P., Kampes B. (2004) A new method for measuring deformation on volcanoes and other natural terrains using InSAR persistent scatterers, *Geophysical Research Letters*, 31, L23611.

Hooper A., Segall P., Zebker H. (2007), Persistent Scatterer Interferometric Synthetic Aperture Radar for Crustal Deformation Analysis, with Application to Volcán Alcedo, Galápagos, *Journal of Geophysical Research: Solid Earth*, 112.

Jaeger J., Cook N., Zimmerman R. (2007), *Fundamentals of Rock Mechanics*, 4th ed., Blackwell Publishing, Maine, US.

Jeremic M. (1994), *Rock Mechanics in Salt Mining*, Taylor and Francis Group, Brookfield, US.

Kratzsch H. (1983), *Mining Subsidence Engineering*, 1st ed. Trans. Fleming R., Springer-Verlag, Berlin Heidelberg.

Lee F., Abel J. (1983), Subsidence from Underground Mining: Environmental Analysis and Planning Considerations, *Geological Survey Circular*, (876).

Lohman R., Simons M. (2005), Some Thoughts on the Use of INSAR data to Constrain Models of Surface Deformation: Noise Structure and Data Downsampling, *Geochemistry Geophysics Geosystems*, 6 (1).

Lugart C., Smith L., Nyahay R., Bauer S., Ehgartner B. (2006), Systematic Technological Innovations Initiative Brine Disposal in the Northeast Final Report, New York Geological Survey & Sandia National Laboratories.

Massonnet D., Feigl K. (1998), Radar Interferometry and Its Application to Changes in the Earth's Surface, *Reviews of Geophysics*, 36 (4): 441 – 500.

Menke W. (1989), *Geophysical Data Analysis: Discrete Inverse Theory*, Academic Press, Inc., San Diego, CA, US.

Nieto A., Young R. (1998), Retsof Salt Mine Collapse and Aquifer Dewatering, Genesee Valley, Livingston County, New York, *Proceedings of the Dr. Joseph Poland Symposium*.

New York State Oil, Gas, and mineral resources 2004 (undated), Annual Report, NYS Department of Environmental Conservation.

Nitti D., Vitis L., Bovenga F., Nutricato R., Refice A., Wasowski J. (2009), Multi-temporal L-band SAR Interferometry Confirms C-band Spatial Patterns of Subsidence in the Ancient Wieliczka Salt Mine (Unesco Heritage Site, Poland), *Proc. FRINGE Workshop*, Frascani, Italy.

Nolan M., Fatland D., Hinzman L. (2003), DInSAR Measurement of Soil Moisture, *IEEE Transactions on Geoscience and Remote Sensing*, 41 (12): 2802 – 2813.

Okada Y. (1985), Surface deformation due to shear and tensile faults in a half-space, *Bulletin of the Seismological Society of America*, 75 (4): 1135-1154.

Perski Z., Hanssen R., Wojcik A., Wojciechowski T. (2009), InSAR Analysis of Terrain Deformation Near the Wieliczka Salt Mine, Poland, *Engineering Geology*, 106: 58 – 67.

Phan X., Ferro-Famil L., Gay M., Durand Y., Dumont M., Morin S., D'Urso G., Girard A. (2012), 1D-Var Multilayer Assimilation of X-band SAR Data into a Detailed Snowpack Model, *The Cryosphere*, 8: 1975 – 1987.

Pierce W., Rich E. (1962), Summary of Rock Salt Deposits in the United States as Possible Storage Sites for Radioactive Waste Materials, *US Geological Survey*, (1148).

Platterner C., Wdowinski S., Dixon T., Biggs J. (2010), Surface Subsidence Induced by the Crandal Canyon Mine (Utah Collapse: InSAR Observations and Elastic-plastic Modelling, *Geophysical J. Int.*, 183: 1089 – 1096.

Prush V., Lohman R. (2014), Forest Canopy Heights in the Pacific Northwest Based on InSAR Phase Discontinuities across Short Spatial Scales, *Remote Sensing*, 6 (4): 3210 – 3226.

Raucoules D., Maisons C., Carnec C., Mouelic S., King C., Hosford S. (2003), Monitoring of slow ground deformation by ERS radar interferometry on the Vauvert salt mine (France) Comparison with ground-based measurement, *Remote Sensing of Environment*, 88: 468 – 478.

Rickard L. 1970: Gamma-ray logs and the origin of salt, *New York State Museum and Science Service*, Pages 34-39, 1970.

Rosen P., Hensley S., Joughin I., Li F., Madsen S., Rodríguez E., Goldstein R. (2000), Synthetic Aperture Radar Interferometry, *Proceedings of the IEEE*, 88 (3): 333 – 382.

Sambeek, L. (2000), An introduction to Subsidence Over Salt and Potash Mining Facilities.

Sambeek, L. (2012), Measurements of humidity-enhanced salt creep in salt mines: Proving the Joffe effect. *Mechanical Behavior of Salt VII*. Ed. Pierre Berest, Mehdi Ghoreychi, F Hadj-Hassan, and Michel Tijani. London: Taylor & Francis Group.

Sandwell D., Myer D., Mellors R., Shimada M., Brooks B., Foster J. (2008), Accuracy and resolution of ALOS interferometry: vector deformation maps of the Father's Day Intrusion at Kilauea, *Transactions on Geoscience and Remote Sensing*, 46 (11): 3524 – 3534.

Sanford K. (1996), Solution Salt Mining in New York, *Northeaster Geology and Environmental Sciences*, 18 (1/2): 97 – 107.

Smith L., Lugert C., Bauer S., Ehgartner B., Nyahay R. (2005), Final Report: Systematic Technical Innovations Initiative Brine Disposal in the Northeast, New York State Museum Culture Education Center.

Swift G., Reddish D. (2005), Underground Excavations in Rock Salt, *Geotechnical and Geological Engineering*, 23: 17 – 42.

S. Yun, P. Segall, H. Zebker. (2006), Constraints on magma chamber geometry at Sierra Negra Volcano, Galápagos Islands, based on InSAR observations, Journal of Volcanology and Geothermal Research, 150: 232-243.

US Salt Precise Level Report Watkins Glen Refinery (2013), Erdman Anthony Project 1001V.80.

Whyatt J., Varley F. (undated), Catastrophic Failures of Underground Evaporite Mines.

Wittke W. (2014), Rock Salt, *Rock Mechanics Based on an Anisotropic Jointed Rock Model (AJRM)*, Ernst & Sohn., Berlin, Germany.

Wosowski J., Bovenga F., Nutricato R., Conte D., Refice A., Kowalski Z., Graniczny M. (2007), Satellite Interferometry Reveals Spatial Patterns of Subsidence in the Ancient Wieliczka Salt Mine (Unesco Heritage Site, Poland), *Proc. Of FRINGE 2007 Workshop*, Frascati, Italy.

Yager R., Miller T., Kappel W. (2001), Simulated Effects of Salt-Mine Collapse on Ground-Water Flow and Land Subsidence in a Glacial Aquifer System, Livingston County, New York, U. S. Geological Survey: Professional Paper 1601.

Yager R. (2013), Environmental Consequences of the Retsof Salt Mine Roof Collapse: U. S. Geological Survey Open-File Report 1174.

Yavuz H. (2001), Yielding Pillar Concept and its Design, *17th International Mining Congress and Exhibition of Turkey*.

Zebker, Howard A., and John Villasenor (1992). Decorrelation in interferometric radar echoes. *Geoscience and Remote Sensing, IEEE Transactions on* 30 (5): 950-959.